May 1998 • NREL/SR-520-24741

Experimental Study of the Factors Governing the Staebler-Wronski Photodegradation Effect in a-Si:H Solar Cells

Final Subcontract Report

D. Han
University of North Carolina
Chapel Hill, North Carolina

National Renewable Energy Laboratory
1617 Cole Boulevard
Golden, Colorado 80401-3393
A national laboratory of
the U.S. Department of Energy
Managed by Midwest Research Institute
for the U.S. Department of Energy
under Contract No. DE-AC36-83CH10093

NREL/SR-520-24741 • UC Category: 1262

Experimental Study of the Factors Governing the Staebler-Wronski Photodegradation Effect in a-Si:H Solar Cells

Final Subcontract Report

D. Han
University of North Carolina
Chapel Hill, North Carolina

NREL technical monitor: B. von Roedern

National Renewable Energy Laboratory
1617 Cole Boulevard
Golden, Colorado 80401-3393
A national laboratory of
the U.S. Department of Energy
Managed by Midwest Research Institute
for the U.S. Department of Energy
under Contract No. DE-AC36-83CH10093

Prepared under Subcontract No. XAN-4-13318-09
May 1998

NOTICE

Available to DOE and DOE contractors from:
Office of Scientific and Technical Information (OSTI)
P.O. Box 62
Oak Ridge, TN 37831
Prices available by calling (423) 576-8401

Available to the public from:
National Technical Information Service (NTIS)
U.S. Department of Commerce
5285 Port Royal Road
Springfield, VA 22161
(703) 487-4650

Printed on paper containing at least 50% wastepaper, including 20% postconsumer waste

PREFACE

This final Technical Report covers the work performed by UNC-CH for the period July 7, 1994 to Jan.15, 1998 under subcontract No. XAN-4-13318-09.

The following personnel participated in the research program:

Jenathan Baugh, X.H. Geng, Daxing Han (P.I.), T. J. Stephen, Keda Wang, Lei Wu, and C. N. Yeh.
The samples were obtained from Team members, L. Y. Yang at Solarex, X. M. Deng at ECD, S. Hegedus at Institute for Energy Conversion (IEC) at Delaware, and a-Si group at NREL.

Over last three and a half years, we have benefited from numerous discussions and cooperation with our Condensed Matter colleagues at UNC-CH, Prof. L. E. McNeil, Prof. Y. Wu. At other institutions we have collaborated with: Liyou Yang at Solarex, with Xunming Deng at Energy Conversion Devices (ECD), with S. Nitta, Gifu University Japan, and mostly with Qi Wang, B. von Roedern, A. H. Mahan and R. S. Crandall et al. at National Renewable Energy Laboratory (NREL). Our research has resulted in the publications of 22 papers (see publications) and the submission of three annual reports.

Page
Intentionally
Blank

TABLE OF CONTENTS

LIST OF FIGURES

SUMMARY

Our goal is to help the U. S. amorphous silicon PV industry to achieve the U.S./DOE PV Program milestone of 12% stable efficiency modules by 1998.

We have concentrated on determining the hydrogen microstructure controlling the stability in a-Si:H materials, on the recombination mechanism of the injected carriers in a-Si:H p-i-n structures, and the correlation of the internal electric field profile to the solar cell performance.
During the contract years, July 7, 1994 to Jan.15, 1998, we summarized systematical studies of the electroluminescence (EL) in a-Si:H p-i-n devices; we have measured the internal electric field profile $E_i(x)$ in p-i-n and n-i-p cells by a null-current method; we studied the structure of the hydrogen clusters in hot-wire a-Si:H films both theoretically and experimentally; and we also started film stress measurements.

We have developed a complete model to explain the features of the electroluminescence (EL) as dispersive-transport-controlled non-geminate recombination processes. This model can explain the main features of the EL not only in a-Si but also in other types of trap-rich materials. The results will be given in section I.

In section II we present our results of the internal field profile, $E_i(x)$, studies in H-diluted and non-diluted p-i-n ells, and p-i-n and n-i-p structures.

Section III explores the microstructure origin which leads to more stable new a-Si:H materials. We show a clear evidence of improved structural order in hot filament assisted CVD a-Si:H, which is an important factor leading to more stable materials.

Section IV

Our research for the last year and a half has resulted in seven publications, and one submitted paper. We submitted four quarterly reports, one final subcontract report, one annual technical report, and reports for the team meetings.

INTRODUCTION

This report describes the research performed during the three and a half year project (July 7, 1994 to Jan.15, 1998) under NREL Subcontract No. XAN-4-13318-09. It covers mainly the most recent work, while the results have been published in Annul Reports for the earlier Phases.[1-3]

The central unsolved problem in the study of hydrogenated amorphous silicon (a-Si:H) is the metastability. It was shown that dangling bond (DB) defects, which cause inferior properties of a-Si:H, are created upon light soaking and can be removed by annealing. The microscopic origin of such metastability is still unclear. Until very recently, device quality a-Si:H films prepared by various techniques exhibit very little differences in structural and physical properties such as metastability. This situation has changed as a result of two new major advances in this field. One is the demonstration that H-dilution during the conventional glow discharge (GD) film growth improves the stability of a-Si:H. The second is the demonstration that a-Si:H produced by the hot filament assisted chemical vapor deposition technique (hot wire) has significantly improved stability and low DB density; it needs only 1-3 at.% H to minimize the DB density compared to the 8-10 at. % H in the conventional device quality GD materials.

We have focused on the H-dilution/non-dilution of p-i-n cells and the hot-wire films to explore (1) what is the carrier transport/recombination mechanism in a-Si:H solar cells and (2) what is the linkage between hydrogen microstructure and metastability? This information is lacking. Understanding these linkages would be an important ingredient in understanding the actual degradation mechanism.

The purpose of our research is to address the above questions through studies of EL, electric field profiles on p-i-n solar cells, and of proton NMR and film stress in new a-Si:H materials.

1) Electroluminescence (EL)

EL is a result of carrier radiative recombination in the intrinsic-layer of p-i-n solar cells. The emission photon energy depends on the carrier distribution in the localized states. By studying the temperature and applied field dependencies of the forward current, the EL efficiency, and the EL spectra, we have developed a complete model to explain the unique features of the EL from trap-rich materials.

2) Internal Electric Field Profiling, $E_i(x)$

The electric field profile varies depending upon where recombination takes place. We have started to study the effect of hydrogen-dilution on $E_i(x)$ and measured $E_i(x)$ in a-Si:H p-i-n and n-i-p solar cells.

3) NMR

Since Si-H bonds play an important role in the metastability, we have done an NMR investigation of H cluster configurations in a-Si:H both experimentally and theoretically.

RESULTS

I. Electroluminescence (EL) in a-Si:H p-i-n cells: dispersive-transport-controlled recombination

I.1 Introduction

The performance of a-Si:H solar cells is believed to be determined, to a large extent, by the carrier recombination via the gap states (DOS) in the intrinsic i-layer. Electroluminescence (EL) has been used to study localized states and recombination processes of the intrinsic layer in a-Si:H p-i-n structures. EL arises from recombination of non-geminate e-h pairs because the electron and hole are injected from opposite sides of the diode. In earlier EL studies,[4-6] other authors argued that the PL and EL were identical except for the low EL efficiency and the lower EL peak energy position. The latter was explained by optical interference effect.[4] The same researchers suggested that the low EL efficiency is due to the fact that the recombination only takes place near the p-i interface. Except for the geminate process in PL,[7-10] one would expect similar recombination processes in both EL and PL, i. e., regardless of the generation methods. However, significant differences in the features of EL and PL in the same p-i-n or n-i-p structures have been observed. We have explained[1-3,11], that the EL efficiency is as high as the PL efficiency, and that the recombination takes place within the whole i-layer because the carriers' lifetime is much longer than the transit time in conventional a-Si:H p-i-n and n-i-p diodes. We further studied the temperature and electric field dependence, as well as the light-soaking effect. Based on systematic studies,[11-13] we have developed a complete model to explain the features of the EL as dispersive-transport-controlled non-geminate recombination processes. This model can explain the main features of the EL not only in a-Si but also in other types of trap-rich materials.

I.2 Samples and experimental conditions

Device quality a-Si:H p-i-n diodes were made on transparent-conducting-oxide (TCO) coated-glass and n-i-p on TCO coated-stainless-steel substrates by plasma-enhanced chemical vapor deposition (PECVD), and p-i-n diodes by photo-enhanced CVD techniques. The TCO was textured to avoid interference fringes, except for one pair of 1.0 mm thick identical samples deposited on both textured and smooth surfaces that were used to insure that the structure of the EL spectrum is not due to optical interference effect. The top contacts were Ag, Al or ZnO, the area was 0.1 to 0.3 cm^2. The i-layer thicknesses L were 0.2, 0.3, 0.4, 0.5, 0.53, 0.55, 1.0, 1.1, 2.0 and 10.0 mm. Samples with $L \leq 0.55$ μm are called thin samples while L □ 1 μm are called thick samples. Among them, high performance a-Si:H p-i-n solar cells were made by d.c. glow discharge at Solarex.[14] The 0.5 μm intrinsic layers were made of either hydrogen-diluted silane or pure silane, denoted as p-i_H-n and p-i-n, respectively. The sample preparation conditions and cell performance furnished by the fabricating laboratories are given elsewhere.[11]

States A and B denote the initial and the photo-degraded state of the p-i-n diode, respectively. The photo-degraded state was reached by exposure of the sample to a 200 mW/cm^2 white light with an infrared-cut-off filter. From eight to one thousand hours light-soaking through the glass side of the sample was used to reach State B.

An Ar-ion laser with output power of 0.25-3 W/cm^2 at 514.5 nm was used for PL excitation. The corresponding absorption depth is 800 Å in an undoped a-Si:H. For EL measurements, the applied voltage was obtained from a programmable pulse generator. 10 Hz repetition rate with 10 ms pulse width were typically used. We varied the forward bias current density between 10^{-4} to 10^2 mA/cm^2. The contribution of thermal radiation to the signal was less than 2% of the total signal.[11] The EL efficiency temperature dependence was measured under constant voltage conditions. The emitted photons were dispersed in a monochromator and detected by a liquid-nitrogen-cooled Ge detector through the glass side of the samples. A lock-in technique was used to collect the PL or EL luminescence signal. The response curve of the detector and the system optics were calibrated with a linear response detector.

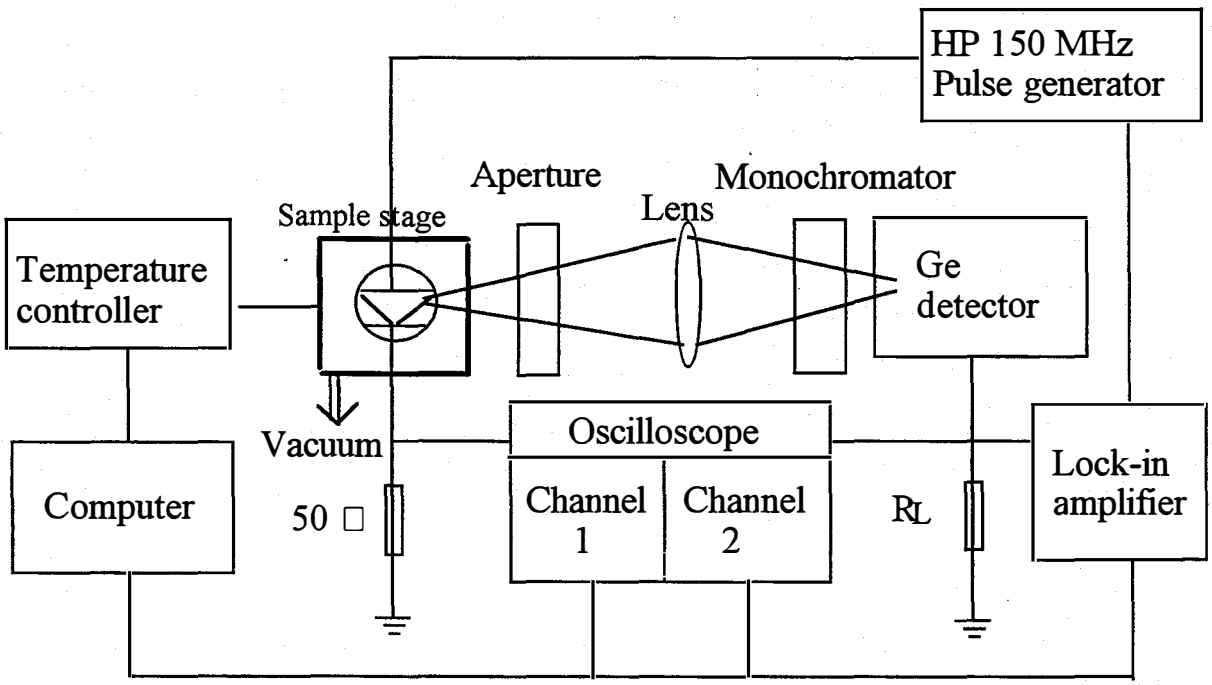

Fig. 1 EL Experimental Layout

I.3 EL results

A. The critical energies of carrier transport and recombination in trap-rich materials

In amorphous semiconductors, the continually distributed localized states affect the recombination processes as well as the transport. It is commonly accepted that the carrier transport in disordered materials is trap-limited and it can be described by the so-called multiple trapping (MT) model,[15,16] in which the carriers are frequently trapped in tail states and released by thermal excitation. In the MT model the carrier transport is considered to take place at the mobility band

edge, and at certain times, the average trap energy of the carriers is given by the demarcation level E_D,

$$E_D = kT\ln(\nu_0 t). \qquad \text{when } T < T_0 \qquad (1)$$

E_D is defined as the energy at which the thermalization rate (ν_0) is equal to the reciprocal of the observation time (t) in carrier transport measurement.[12,13] The deepest energy position of the demarcation energy E_D is the bottom of the tail states, that is about 0.3 - 0.35 eV above E_v and 0.1 - 0.15 eV below E_c for the holes and electrons, respectively. The phonon-assisted transition rate (thermalization rate) ν_0 ♠10^{12} s^{-1} is greater than both the radiative- and nonradiative recombination rate, 10^3 - 10^4 s^{-1} and 10^6 - 10^7 s^{-1}. The luminescence therefore occurs only after the majority of carriers have thermalized to sufficiently low density of states that further phonon-assisted transitions are suppressed by the weak overlap to neighboring sites. The tail-to-tail luminescence peak energy reflects the carrier distribution in the tail states and is expected to have a time- and temperature shift of the peak energy. The thermalization model is also used to explain the temperature dependence of PL efficiency and to deduce the valence band tail width by using the carrier's average lifetime (τ_r) instead of the observation time t as shown in Eq. (1).

In the case of EL, we found that both the energy peak position (EL_{peak}) and its temperature dependence do not follow the thermalization model, especially at low temperatures. We suggest that carrier transport has to be considered as determining factor. The MT model provides a good description of the transport phenomena for temperature greater than ~ 200 K. At lower temperatures, hopping transport in the exponential band tail (or through potential fluctuations) must be considered. The carrier transport then is no longer near the band edge E_c (E_v) but at transport level (E_t) that has been introduced by Monroe.[17]

$$E_t = kT_0 \ln(8/27R_0^3N_0) - 3kT_0 \ln(T_0/T). \qquad (2)$$

where R_0 is the effective Bohr radius, and N_0 is the density of states at the initial energy E. The first term is an energy which is estimated to be close to the mobility edge, so that the second term represent the shift of the transport path below E_c (above E_v for holes). Both hopping-up and hopping-down processes are permitted within band tails at about T > 200 K, below this temperature only hopping transition to states of lower energy occur.[14] At about T > 200 K the second term in Eq. (2) becomes very small, thus E_t ♠ E_c (♠ E_v for holes) and the MT model is valid. When the band-tail distribution is broad (a greater T_0) and at low temperatures such that T < T_0 the electron transport level shift below E_c (above E_v for holes) is most significant. Furthermore, in the dispersive regime (T < 200 K for electrons, T < 350 K for holes), it has been found that the carrier drift mobility increases as the field increases, in the same manner as it increases with increasing temperature.[18] In other words, the carriers transport level shifts towards the band edge with increasing electric field in that temperature range.

First we discuss the role of the critical energies $E_D(T)$ and $E_t(T)$ in the forward bias current. The steady state forward current in a-Si:H p-i-n and n-i-p diode is a recombination limited current. We discuss the applied-field range of 2-10 ∞ 10^4 V/cm in which both the recombination-rate and

the current spatial distribution are uniform through the i-layer according to a numerical calculation.[19] Hence, one can obtain the properties of the i-layer from the measurements. The dominant factor that determines the forward current behavior is the conduction band tail because the electrons move much faster than the holes. Thus, the forward current density is $J_F \cong J_n = \mu_n \tau_n E$. One can obtain the electron transport parameter, the mobility-lifetime product $m_n t_n(T)$, from the $J_F(T)$ curves. Fig. 2a shows the calculated $E_D(T)$ and $E_t(T)$ positions as a function of temperature for electron according to Eqs. (2) and (3) by using $\nu_0 \tau_r = 10^5$ (with a non-radiative recombination lifetime $\tau_r = 10^{-7}$ s) and T_0 = 300 K. The transport level $E_t(T)$ represents the balance of hopping and thermal excitation to $E_t(T)$; it shifts to the band edge as there is an increasing of temperature. The demarcation level $E_D(T)$, on the other hand, represents the balance of thermal excitation to the band edge and retrapping into the tail states; it shifts away from the band edge as there is an increase of temperature. Considering the increase of the electric field in the same manner as an increase of temperature, we calculated the transport levels, $E_t(T)$, at electric field equal to 2, 4, and 6, $\infty 10^4$ V/cm. For a better fit to the experimental results of both the current and the luminescence, we consider the thermalization processes beginning at 80 K in the calculation. There are two transition temperatures, T_{2e} and T_{1e}, in the figure. When $T < T_{2e}$, the transport energy level E_t is deeper than the thermalization energy E_D,

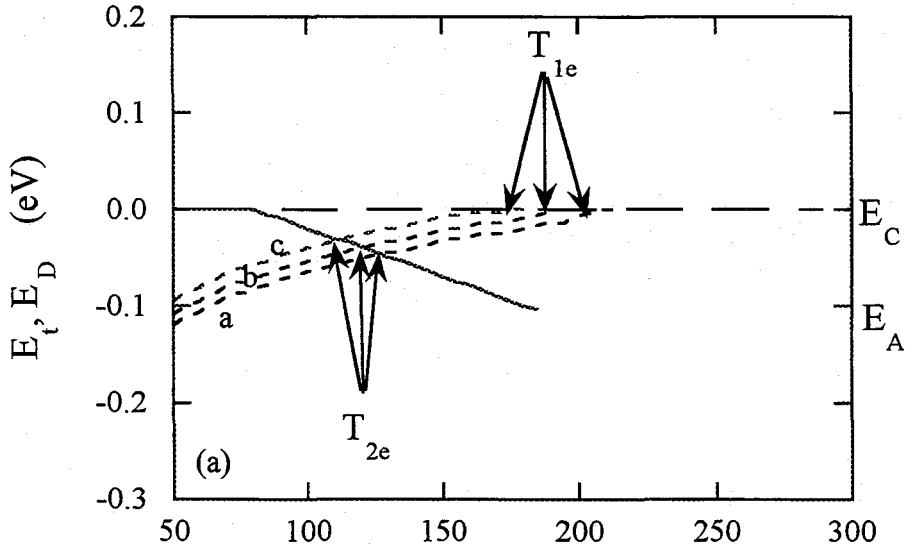

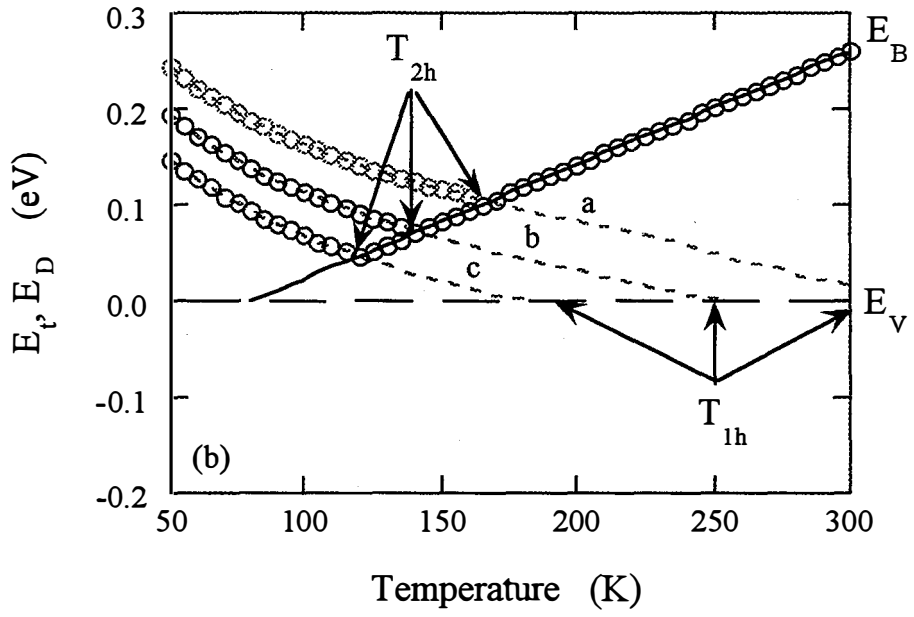

Fig. 2 Calculated $E_t(T)$ and $E_D(T)$ positions as a function of temperature. The solid line corresponds to E_D=-kTln($\nu_0\tau_r$), and the dashed lines correspond to E_t= -$3kT_0\ln(T_0/T)$. E_C and E_A, and E_V and E_B indicate the conduction-band edge and the bottom of the conduction-band tail, the valence-band edge and the bottom of the valence-band tail, respectively. The dashed lines a, b, and c correspond to the electric field 2, 4, and 6 ∞ 10^4 V/cm, respectively.
Figs. 2(a) for electrons using $\nu_0\tau_r = 10^5$, T_0 = 300 K.; 2(b) for holes, using $\nu_0\tau_r = 10^6$, T_0 = 450 K. The open circles indicate the tunneling transition energy for EL_{peak}. The cross point of $E_t(T)$ and $E_D(T)$ indicate the temperature, T_{2h}, where the carrier transport mechanism changes. T_{1h} indicates the temperature where the demarcation level has reached the bottom of the tail.

and electrons move along at E_t. The cross points of $E_t(T)$ and $E_D(T)$, T_{2e} ♠ 110, 120, and 125 K, indicate the temperature where the carrier transport mechanism changes from hopping-controlled to MT regime where the electrons move still along E_t. The other transition temperature T_{1e} ♠ 180, 190, and 200 K, indicates the temperature where the transport energy level has reached the conduction-band edge E_c. Meanwhile, at a temperature of about T_{1e} the electron demarcation level E_D has reached the bottom of the conduction tail E_A. When $T > T_{1e}$, the carriers move along the conduction-band edge; then the carrier transport is in the extended sattes.

We now discuss the role of the critical energies $E_D(T)$ and $E_t(T)$ in the EL. Because the valence band tail is much broader than conduction band tail, the features of the EL are dominated by valence band tail states. According to Eqs. (1) and (2) by using $\nu_0\tau_r = 10^8$ (with a radiative recombination lifetime $\tau_r = 10^{-4}$ s) and T_0 = 450 K for holes. Fig. 2b shows the calculated demarcation energy and transport energy positions as a function of temperature and electric field for holes. At temperatures $T < T_{2h}$, the hopping controlled regime determines carriers transport.

The transport level is deeper in the tail. If the EL_{peak} is controlled by the transport level $E_t(T)$, rather than $E_D(T)$, the peak energy position of EL will be lower. $E_t(T)$ crosses $E_D(T)$ at temperature, T_{2h} ♠ 115, 135, and 155 K, where T_{2h} decreases with increasing electric field. The demarcation energy is deeper than the transport level in this regime, so the radiative tunneling occurs from E_D with high probability and the EL energy peak position will be controlled by the demarcation energy. At T_{1h} ♠ 190, 250, and 310 K the transport level reaches the valence band edge E_V, causing the free carriers to be captured by deep states more efficiently. Thus, recombination via defects will dominate. Meanwhile, at temperature about T_{1h} the hole demarcation level E_D has reached the bottom of the valence tail E_B. This implies that the tail states are in thermal equilibrium with the band edge, thus the probability of the tail-to-tail radiative transition is very low. Consequently, one observes a dominating defect EL for $T > T_{1h}$.

We will see that the features of both the forward current and the EL temperature and electric field dependence as well as the EL energy spectrum in p-i-n structures can be explained by using the temperature dependence of the characteristic energy curves in Fig 2a and 2b.

B. Forward bias current temperature dependence

We show the forward current density J_F temperature dependence data from the thin and thick a-Si:H p-i-n and n-i-p samples in their initial states A. Figs. 3a and 3b show the J_F vs. 1/T curves for a 0.5 μm p-i_H-n diode under 2, 3, and 4 V bias, for a 0.5 μm n-i-p diode at 1.6, 2.4, and 4 V bias, respectively. The electric field across the i-layer is $V_i/L = (V_a - V_{bi})/L$, where V_a is the applied voltage and V_{bi} = 0.8 V is the built-in potential. The general picture of the current temperature dependence shows three regions corresponding to the three regions in Fig. 2a:

(a) $T < T_{2e}$, the low temperature hopping transport regime: the injected carriers move along the transport level E_t that is deep down to the tail states as shown in Fig. 2a. The weak temperature dependence of the current is due to a small activation energy of $\mu_n\tau_n$, that is about 0.01 eV, reasonably for the hopping activation energy.

(b) $T_{1e} < T < T_{2e}$, the multiple-trapping (MT) regime: the transport level E_t is above the demarcation level E_D. The carriers are still moving along at E_t which is very close to E_c. The current is thermally activated with an activation energy which gives the activation energy of m_nt_n. In Fig. 3a, one obtains the transition temperature T_{2e} at 110 -120 K which is consistent with the calculated curves in Fig. 2a. For electric field 2, 4, and $6\infty10^4$ V/cm in the 0.5 μm p-i-n diode, the activation energy is 0.08, 0.095, and 0.13 eV that agree well with the results from electron drift mobility measurements. In Fig. 3b the solid lines are from the n-i-p diode while the dashed lines are from the same p-i-n cell as in Fig. 3a. One can see clearly that the transition temperatures of T_{2e} and T_{1e} shifts to higher temperature, we believe that is due to injection limitation of the contact of the n-i-p diode. A smaller activation energy 0.07 - 0.08 eV is obtained from the 0.5 μm n-i-p than that from the 0.5 μm p-i-n diode. An activation energy ♠ 0.07-0.15 eV was observed for the thin p-i-n and n-i-p diodes. The variation of the activation energy is due to the field dependence of the drift mobility.

(c) $T > T_{1e}$, the transport level E_t has already reached the conduction-band edge E_c. The carrier transport is assumed to be in extended states, thus the current is no longer thermally

activated. However, the dispersive behavior still can be seen in transient measurements. The calculated T_{1e} is about 200 K in agreement with the experimental T_{1e} in Figs. 3a and 3b.

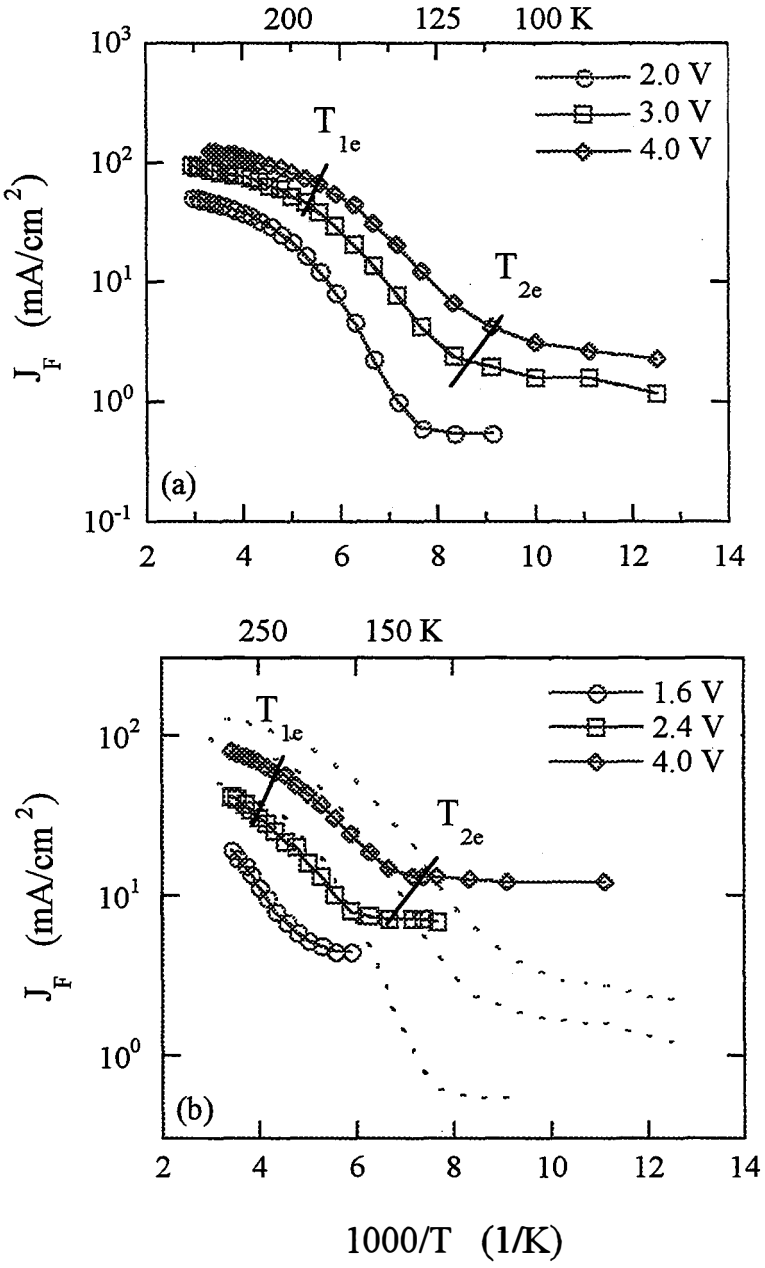

Fig. 3 Forward current density J_F as a function of temperature from (a) 0.5 μm p-i_H-n diode under 2.0, 3.0, and 4.0 V bias; (b) 0.5 μm n-i-p diode under 1.6, 2.4, and 4.0 V, the dashed lines from p-i-n diode in (a). Two transition temperatures T_{1e} and T_{2e} are indicated.

C. EL efficiency temperature dependence

The PL temperature dependence from the p-i-n or n-i-p structures follows the termalization model described in Eq. (1) as the same as that from intrinsic films. However, carrier transport could play a role in the temperature dependence of EL. In order to keep the generation rate constant, in earlier work,[4-6] constant current conditions were used to measure the EL efficiency temperature dependence, i.e. the injected electron density J_F/eL has been used as the generation rate. They found[4-6] a much lower EL efficiency than PL. Our previous studies[1-3,11] have explained that the generation rate of EL is not simply the injected electron density J_F/eL in a-Si:H diodes, but should be written as

$$g = (J_F/eL)\infty(\tau_r/t_o) \cong J_F/e(\mu_n\tau_n E), \qquad (3)$$

or $$g \propto J_F/eL, \qquad \text{when } (\tau_r/t_o) \square 1$$

where J_F is the density of forward bias current, $\mu_n\tau_n$ is the electron mobility-lifetime product, L is the thickness of the i-layer, and t_o is the carrier transit time across the i-layer. $\mu_n\tau_n E = L_d$ (drift-length) should be used instead of the i-layer thickness L in the expression of J_F/eL. Therefore, we have suggested using a constant voltage instead of a constant current condition for the EL efficiency temperature dependence measurements. The limitation for using J_F/eL as the EL generation rate is $(\tau_r/t_o) \square 1$, or $L_d/L \square 1$. The carrier transit time is $t_o = L^2/\mu_n V_i$. The electron transit time is about $2.5\infty10^{-10}$ s with a band-edge mobility $\mu_n \cong 10$ cm^2/Vs across a 0.5 mm thick i-layer, under forward bias 1 V. The gain factor τ_r/t_o then is as large as 10^2 to 10^3 when the electron recombination lifetime is 10^{-6} -10^{-7} s. This explains that the early EL work found a 10^2-10^3 times smaller EL efficiency than the PL efficiency, ignoring the gain factor τ_r/t_o in the generation rate expression, $g = J_F/eL(\tau_r/t_o)$. The hole lifetime is also longer than it's transit time if both the hole lifetime and the hole mobility are one order of magnitude lower than the electron's. Therefore, the injected electrons and holes must circulate through the diode before they find each other and recombine. The electrons circulate 10^2 times more than the holes because of the higher mobility and the longer lifetime. So the carrier recombination take place through the whole i-layer indeed. The above argument about the gain factor will be valid in the temperature range $T > T_2$ where the MT model is valid; in other words, when the carrier transport takes place near the mobility edges. The carrier's mobility will decrease rapidly in the hopping transport regime when $T < T_2$, and then the gain factors tend to be one.

The EL efficiency can be written as the total emission intensity per generation rate per unit area A,

$$y_{EL} = I_{EL}/Ag = (I_{EL}/I_F)\infty e\mu_n\tau_n(V_i/L). \qquad (4)$$

The total emission from the sample is I_{EL}, the forward current is $I_F = AJ_F$. Assuming that a small thermal activation energy of $m_n t_n$ product can be taken into account later, the factor $\mu_n\tau_n(V_i/L)$ does not change with temperature under constant voltage. Thus, I_{EL}/I_F is the effective EL efficiency in temperature dependence measurements under constant voltage condition. In other words, a constant voltage (not a constant current!) with a modification of the activation energy of

$\mu_n\tau_n$ means a constant generation rate in the EL efficiency temperature dependence measurements.

We show the experimental results of EL effective efficiency, I_{EL}/I_F, as a function of temperature for p-i_H-n sample in initial state A in Fig. 4 for a 0.5 μm p-i-n diode. Practically, as temperature increases the rapid increase of current density could break-down the thin film diode, so we have only measured EL efficiency temperature dependence at temperatures near T_{2h} (where the efficiency is maximum) for the 2.0 μm sample. Similar features of the I_{EL}/I_F vs. T curves have been found from all the samples being measured. Interestingly, as temperature increases above 0 K there are three regimes in the I_{EL}/I_F vs. T curves:

(a) $T < T_{2h}$, the efficiency I_{EL}/I_F increases rapidly with temperature and depends on the applied voltage. The EL efficiency shows a maximum value at a transition temperature. T_{2h} and the maximum efficiency vary with applied voltage, higher fields correspond to a lower T_{2h} and higher efficiency.

(b) $T > T_{2h}$, the efficiency I_{EL}/I_F decreases with temperature and does not depend on the applied voltage. It is reasonable that the I_{EL}/I_F vs. T curves do not depend on voltage for $T > T_{2h}$, if the luminescence efficiency depends on the generation rate linearly.

(c) When T is near room temperature, I_{EL}/I_F does not change much with temperature due to the defect EL_d domination. It is shown more clearly in Fig. 4 at T > 250 K.

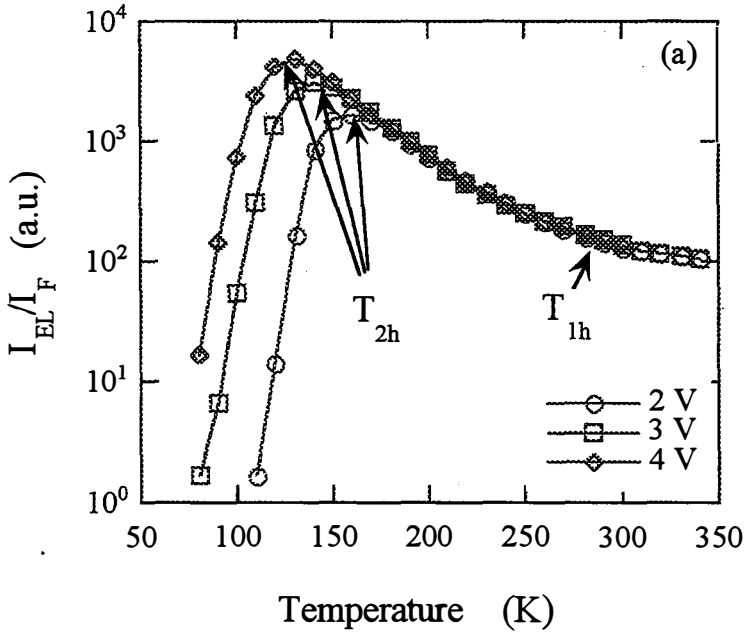

Fig. 4 EL effective efficiency I_{EL}/I_F as a function of temperature for a 0.5 μm p-i_H-n diode at 2.0, 3.0, and 4.0 V bias, the transition temperatures T_{1h} and T_{2h} are indicated.

We have mentioned above that the hole distribution in the valence band tail is the dominant factor for the luminescence signal, and the tail-to-tail transitions dominate the integral EL efficiency at low temperatures. Thus, we explain the experimental results in Fig. 4 by the calculated curves in Fig. 2b for holes. First, for $T < T_{2h}$ one expects the transport to be hopping-controlled. As the temperature decreases, the deeper the transport level, the less the wave function overlap; hence the tunneling rate (r) for the radiative recombination decreases exponentially according to $\rho = \nu_0 \exp(-2R/R_0)$ where R is the average electron-hole separation and R_0 is the effective Bohr radius. It is worth mentioning here that this field-enhanced transition can only be seen in the case of non-geminate recombination. An opposite situation occurs in geminate recombination processes such as the field quenching in PL.[9] It has been found that the carrier drift mobility increases as the field increases in the same manner as it increases with temperature.[18] In other words, the carriers move faster as the field increases. So one would predict that under a higher field the carrier transport would change to MT regime at lower temperature. The EL efficiency temperature dependence curves suggest that T_{2h} ♠ 125 K, 135 K and 150 K for applied voltage 2 V, 3 V, and 4 V, respectively, for the 0.5 μm p-i_H-n diode of Fig. 4. In addition, as predicted by the calculated data in Figs. 2a and 2b, for the same diode the transition temperatures for holes, T_{1h} and T_{2h} are both higher than T_{1e} and T_{2e} for electrons because the much wider valence band tail than conduction band tail. This can be seen clearly in Figs. 3a and 4 for the same 0.5 μm p-i_H-n diode, for instance, T_{1h} and T_{2h} at 2 V are 150 K and 250 K both higher than T_{1e} and T_{2e} at about 120 K and 220 K.

When $T > T_{2h}$, the EL effective efficiency I_{EL}/I_F decreases with temperature similar to the PL efficiency that follows the thermalization model shown in Eq. (1). It is clear that the transition temperature T_{2h} depends on the applied field. In Fig. 5, we plot the T_{2h} as a function of the electric field from a group of a-Si:H p-i-n diodes from several diodes. One can see that the data show that the reciprocal of T_{2h} is proportional to the field, and in a good agreement with the field effect on the carrier dispersive-transport.

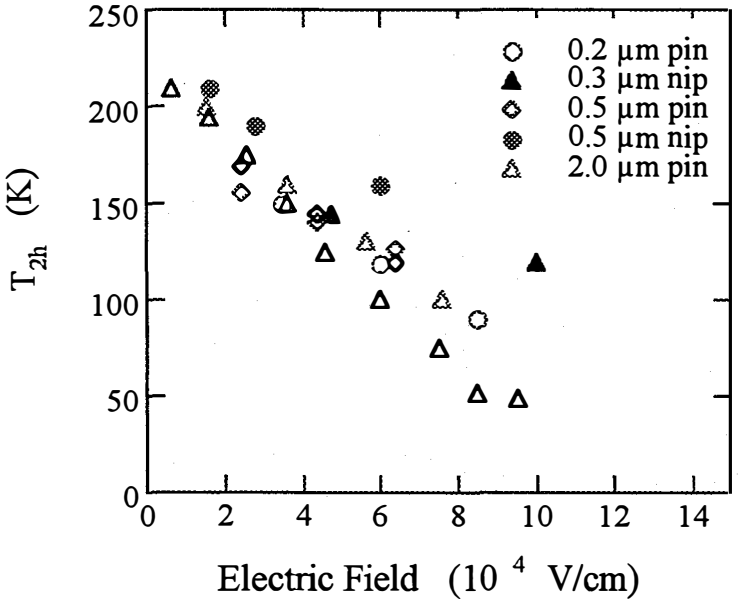

Fig. 5 T_{2h} as a function of the electric field across the i-layer for 0.2, 0.3, 0.5, and 2.0 μm p-i-n and n-i-p samples.

D. Temperature and electric field dependence of the EL energy peak position

It has been a puzzle why the EL peak energy has always been observed to be lower than the PL peak energy of the same sample.[4-6] In Fig. 6, we plot the main-band luminescence peak energy as a function of temperature for both PL_{peak} and EL_{peak} from 0.2, 0.4, and 2.0 μm p-i-n diodes. One can see that the $PL_{peak}(T)$ follows the thermalization model as described in Eq. (1), while the $EL_{peak}(T)$ does not. The PL spectra were measured by 0.1 W/cm^2 514.5 nm laser excitation, and the EL spectra were measured under $2\infty10^4$ V/cm applied field. It is clearly shown that the $EL_{peak}(T)$ temperature dependence is weak in a wide temperature range of 50 K to 300 K.

We have shown that the carrier transport plays a role in the features of the EL temperature dependence. The EL peak energy position also can be discussed according to the characteristic energies shown in Fig. 2b. Since the carrier's hopping rate is much faster than the recombination rate, the carriers first hop down to their transport energy level and circulate many times through the device before recombining from their transport levels. Therefore, when $T < T_{2h}$, the EL_{peak} is controlled by the transport level $E_t(T)$ which is about 0.2 eV deeper than the energy position of $E_D(T)$ at low temperatures. As temperature increases, when $T > T_{2h}$ the energy position of $E_D(T)$ is lower than $E_t(T)$, the transition then occurs between the $E_D(T)$ with higher probability. Thus EL_{peak} will follow the thermalization model similar to that in PL. The open circles in Fig. 2b indicate the possible favorable transition energy for EL_{peak}. It shows a much weaker temperature dependence than that of $E_D(T)$. Therefore, $EL_{peak}(T)$ has weaker temperature dependence than $PL_{peak}(T)$. So both the lower EL peak energy position and its weaker temperature dependence are explained by dispersive-transport-controlled recombination.

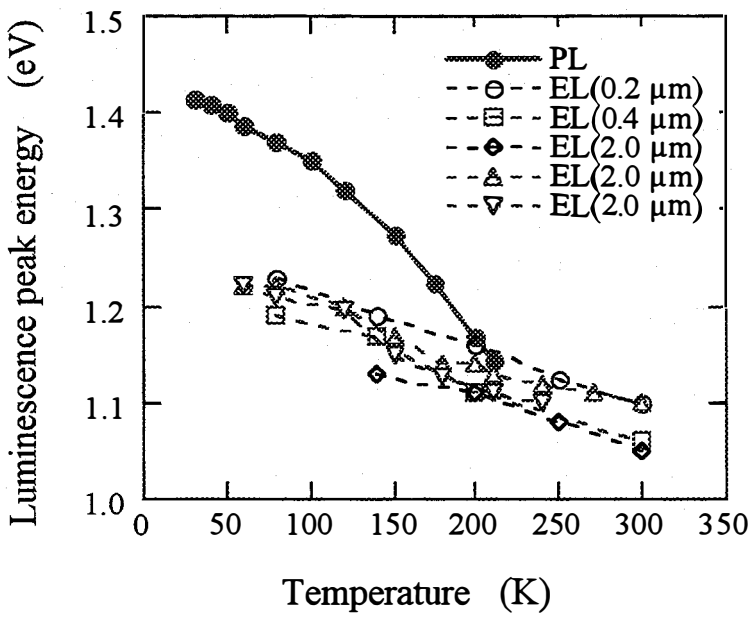

Fig. 6 Comparison of the luminescence peak energy as a function of temperature between PL_{peak} and EL_{peak} from 0.2, 0.4, and 2.0 μm p-i-n diodes.

More evidence of the dispersive-transport-controlled recombination is seen in the EL_{peak} field dependence. At low temperature the EL_{peak} shifts to a higher energy as the electrical field increases as shown in Fig. 7 for a group of p-i-n samples at 100 K. A similar shift was observed at 90 K and 140 K. However, we have not observed a shift of the EL_{peak} with increasing electrical field at T > 200 K. Again, the results agree with the field dependence of the carrier dispersive-transport.[15] That is, the higher the field the closer the transport level is to the mobility edge, so the higher the transition energy for the EL peak position in the dispersive-transport regime.

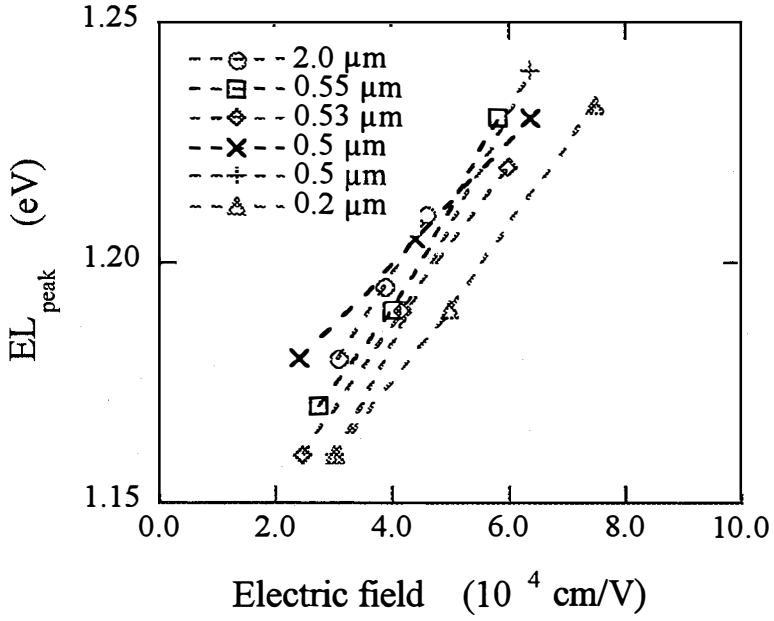

Fig. 7 EL_{peak} as a function of the electrical field for 0.2, 0.5, 0.53, 0.55 and 2.0 μm p-i-n samples at 100K.

E. Light-induced metastable effects

In the above sections, we presented the data of the original state A. The same measurements were done after light-soaking. One of the light-induced changes in a-Si:H sample is the increase of the density of silicon dangling bonds (DBs) that reduces the carrier's recombination lifetime. DBs act as both radiative and non-radiative recombination centers. The defect band dominates the EL spectrum at room temperature. Light-induced metastable changes of the defect EL spectra reflect the metastable changes of the deep states. The light-induced degradation effect has been studied by defect EL spectroscopy, as reported previously. [1-3,11] Here we report the light-induced effects on the localized tail states as well as the dominating effects on carrier transport.

Figs. 8a and 8b show the forward current density J_F temperature dependence for 0.5 μm p-i_H-n and p-i-n cells at state B after 30 h light-soaking. The dashed lines indicate the data from the same samples at initial state A. The light-induced effects are:

(a) an increase of the current density at low temperature hopping transport regime $T < T_{2e}$;

(b) an increase of the activation energy at $T_{1e} < T < T_{2e}$, which reflects an increase of the separation between E_c and the bottom of the conduction band tail E_A;

(c) no obvious change in the temperature range $T > T_{1e}$ where the carrier transport in steady-state is non-dispersive.

The light-soaking effect on EL effective efficiency for the same group of cells before and after light-soaking is shown in Figs. 9 a and b. Interestingly, there are no obvious changes of the EL effective efficiency upon light-soaking in both the H-diluted and non-diluted samples when $T > T_{2h}$. This can be understood since the light-induced metastable change is contained in the transport parameter, $\mu_n\tau_n$, but does not show in the radiative-recombination processes. In previous work [11] we have shown that if the $\mu_n\tau_n$ product is included, i. e., $\mu_n\tau_n(A) \spadesuit 10^{-5}$ cm^2/V at State A, and $\mu_n\tau_n(B) \spadesuit 10^{-6}$ cm^2/V at State B, the EL efficiency shown in Eq. (4), $\mu_n\tau_n I_{EL}/J_F$, does decrease roughly an order of magnitude upon light-soaking. The factor of $\mu_n\tau_n$ is excluded in the EL effective efficiency I_{EL}/I_F, so the light-induced effect cannot be seen in the temperature dependence in Fig. 9. When $T < T_{2h}$, the lower EL effective efficiency after light-soaking could be related to the lower position of the transport level.

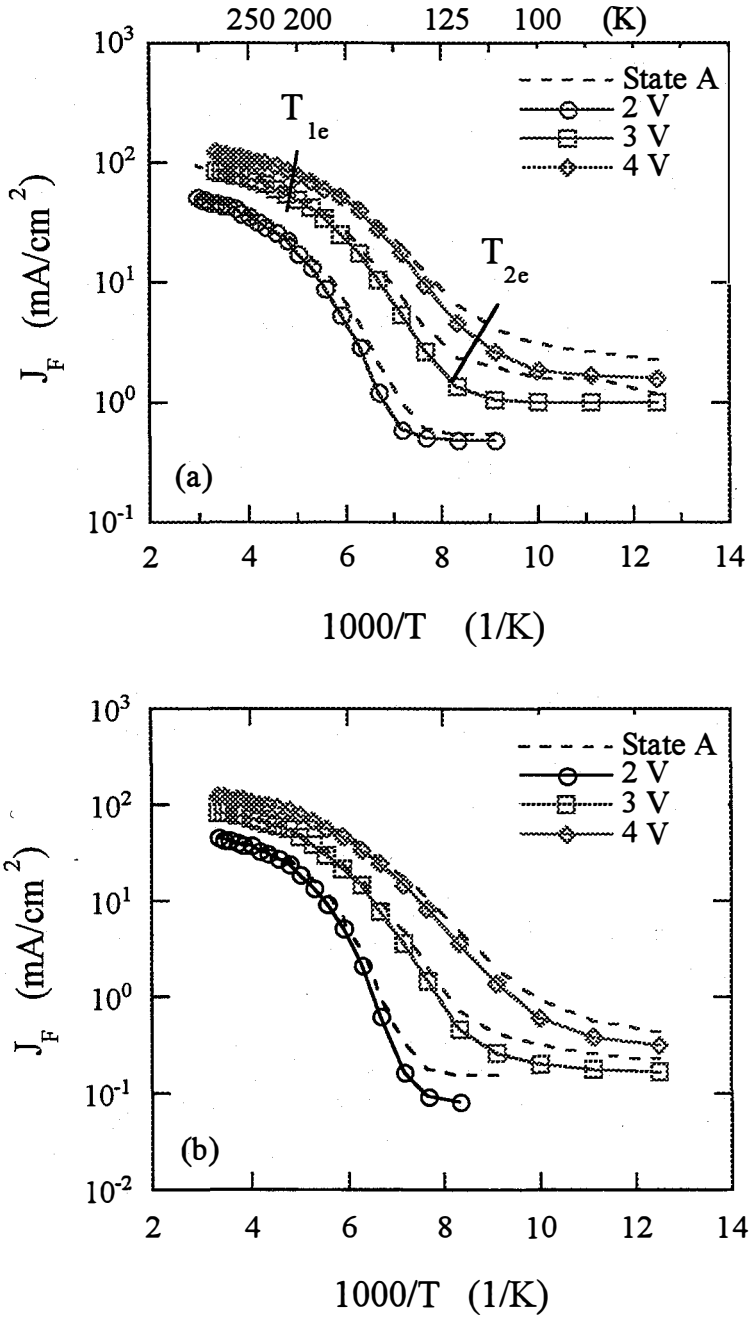

Fig. 8 Light-soaking effect on J_F vs. 1/T curves from 0.5 μm thick (a) p-i_H-n, and (b) p-i-n cell at 2.0, 3.0, and 4.0 V bias. The dashed lines correspond to the data at state A.

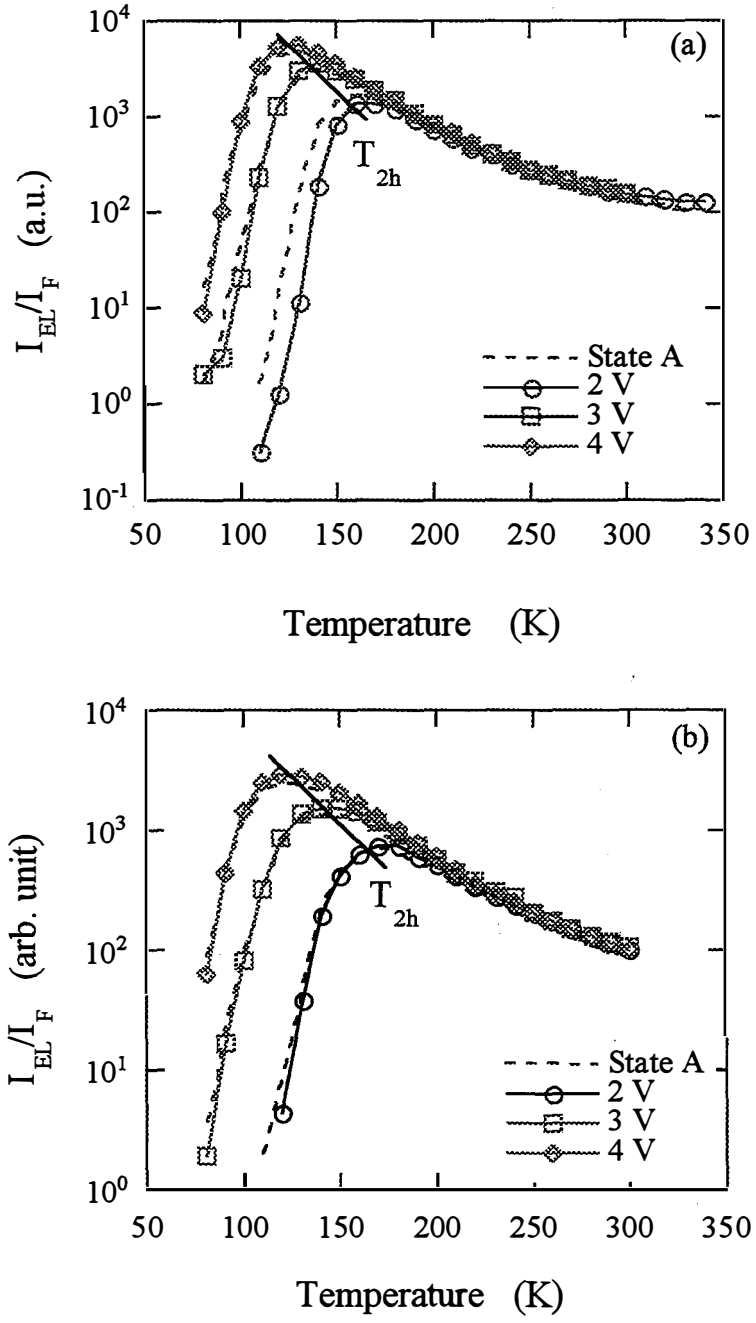

Fig. 9. Light-soaking effect on I_{EL}/I_F vs. 1/T curves from 0.5 μm (a) p-i_H-n, and (b) p-i-n cell at 2.0, 3.0, and 4.0 V bias. The dashed lines correspond to the data at state A.

I. 4 Conclusions

The main conclusions that we draw from these EL studies are:

Both the current and the EL efficiency show three regions according to the transport mechanisms of either hopping-controlled or multiple-trapping, or ballistic (non-dispersive). Compared to photoluminescence (PL), significant differences in the features of EL were observed: (1) the EL main-band energy peak, EL_{peak} ~ 1.2 eV, is always 0.1- 0.2 eV lower than PL_{peak}; (2) the PL peak energy decreases with increase of temperature, whereas the EL main-band peak energy hardly changes with temperature but changes with applied voltage; (3) at low temperatures, the PL intensity I_{PL} is quenched but the I_{EL} is enhanced by electric field; (4) the PL efficiency decreases with increasing temperature when T > 50 K, but the EL effective efficiency I_{EL}/I_F increases rapidly with temperature and shows a maximum at a higher temperature T_{2h} (100 - 200 K), finally, (5) the defect-band intensity is four order of magnitude weaker than the main-band intensity in the case of PL at low temperatures whereas it is less than two order of magnitude weaker in thin p-i-n structures in the case of EL.

In amorphous semiconductors the localized state distribution affects both the recombination processes and the transport. The main difference of the EL main-band from PL is that carrier transport is involved under double injection. In the case of PL, the recombination is a thermalization-controlled geminate process whereas in the case of EL, the recombination is a dispersive-transport-controlled non-geminate process. However, when the demarcation energy is deeper than the transport-level at $T > T_{2h}$, both the thermalization of the carriers in the valence-band tail states and the transport processes are involved in EL. The origin of the temperature dependence of the transport parameter $\mu_n\tau_n(T)$ can be attributed to the thermalization of the electrons in the conduction band-tail states. Therefore the features of both PL and EL intensity temperature dependence, I_{EL}/I_F, and I_{PL} vs. T are similar. If the temperature dependence of the transport parameter $\mu_n\tau_n(T)$ is taken into account, the width of the valence-band tail kT_0 can be deduced from $(I_{EL}/I_F) \propto \mu_\nu\tau_\nu(T)$ vs. T curve according to Eq. (1).

By employing the forward current and EL temperature dependence studies information of both the localized tail states and the deep defect states in real solar cell structures were obtained concomitantly, that is crucial for the device performance. In thin p-i-n diodes the defect EL intensity is two order of magnitude stronger than that in the case of PL, so the room temperature EL spectroscopy has been used to study photodegradation kinetics in solar cells.[14] One of the advantages of these studies, as compared to PL, is that the properties of the entire i-layer are obtained, because the recombination takes place through the whole i-layer in EL, but the PL signal is limited by the absorption depth of about 400-800 Å. The other advantage is that the low EL main-band peak energy due to dispersive-transport-controlled recombination allows us to explore the deeper tail states. In previous studies[8-11] of the EL defect spectra in p-i-n cells, we have reported that both the defect-state and tail-state energy distribution in the i-layer have been modified by hydrogen-dilution treatment. In this study, we have found more evidence of the light-induced metastable increase of the $\mu_n\tau_n$ activation energy and the changes of the EL main-band spectrum lineshape, that indicate a light-induced band tail broaden, especially the deeper part of the tail states.

II. Internal electric field profile in p-i-n cells studied by the transient-null-current method

II.1 Null-current method

Since the charge collection process in a-Si:H based solar cells depends upon field-assisted drift in the internal-electric-field, experimental knowledge of the internal-electric-field profile is important for high efficiency and stable device design. One needs to know how the electric field distribution affects the V_{oc}, the quantum efficiency wavelength dependence, and to determine how the electric field changes upon light-soaking. By using computer simulation, the physics, and the relation of the electric field distribution with V_{oc} of a-Si based alloy p-i-n cells under steady state light illumination have been studied by Hack et al [19-21] and Fonish et al [22]. When there is a constant midgap state (MGS) and the free carrier density is negligible, from Poissons equation one obtains that the electric field $E_i(x)$ decays exponentially from the junction interface,

$$E_i(x) = E_0 e^{-\beta x} \qquad (5)$$

where $\beta^{-1} = L_o$ is the decay length (the Debye length). $\beta = 1/L_o = q(MGS/\varepsilon)^{1/2}$ where $q=1.6\times10^{-19}$ C and $\varepsilon=1\times10^{-12}$ F/m. The value and the decay rates depend on the space charge density and the carrier's mobility (see the results of numerical calculations[19-21]). On the other hand, a few experimental results have been published.[23-26] Among them the transient-null-current method is an attractive technique because the experimental knowledge of $E_i((x)$ can be obtained in a real p-i-n cell structure. We report the experimental results of $E_i((x)$ on a-Si:H and a-SiGe:H solar cells with varied i-layer thickness.

According to the early works of the null-current technique in a-Si solar cells, [23,24] the transient photocurrents generated by a low-intensity pulsed laser were tuned to zero by the forward-bias voltages and consequently the internal electric field profile can be determined.

$$j_{pc} \propto \int_o^L [E_i(x) - V_a/L] e^{-\alpha(\lambda)x}\, dx = 0 \qquad (6)$$

where Va at null-current condition can be measured as a function of wavelength λ. The field profile $E_i(x)$ then can be found by the best fit to the experimental data according to Eq.(6). We use a field-distribution function in the form of $E_i(x) = E_0 e^{-\beta x} + E_1$ for the field profile near the p-i interface.[19,23] Inserting this $E_i(x)$ into Eq. (6) one obtains

$$\int_o^L [(E_0 e^{-\beta x} + E_1) - V_a/L] e^{-\alpha(\lambda)x}\, dx = 0 \qquad (7)$$

With known $\alpha(\lambda)$ one finds the fitting parameters to the experimental data of V_a (λ) by solving the integral.

A HP 8110A 150 MHz pulse generator with $1\infty10^{-11}$ sec resolution was used to apply a positive voltage pulse. For the photoexcitation, a short laser pulse $t_{pl} \sim 2\infty10^{-10}$ sec with varied wavelength of 380 - 640 nm was used. Neutral density filters were used to adjust the incident light flux. The experimental error was ± 0.05 V. The measurements were made at room temperature. A schematic diagram of the experimental apparatus is shown in Fig. 10.

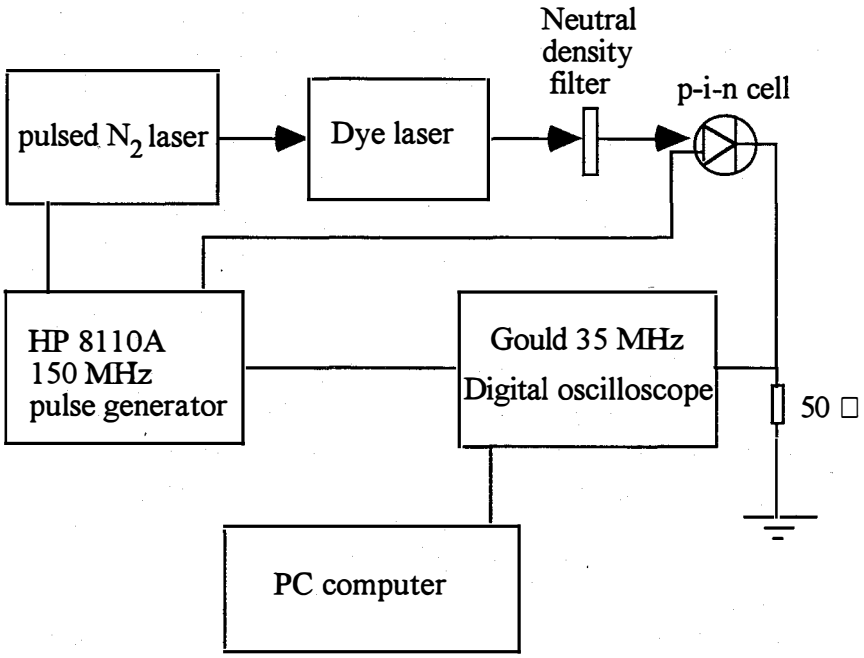

Fig. 10 Block diagram of the transient-null-current experimental apparatus.

II.2 $E_i(x)$ results

Samples were made by plasma-enhanced CVD. Several structures were studied i.e. 0.5 μm a-Si Glass/CT/p-i-n/Al and Glass/CT/n-i-p/Al cells. A 150 MHz pulse generator with $1\infty10^{-11}$ sec resolution was used to apply a positive voltage pulse. For the photo excitation, a pulse-N_2-laser-pumped dye laser in a wavelength range of 380-640 nm was used. Neutral density filters were used to adjust the incident light flux. The measurements were made at room temperature. The detail experimental conditions can be found elsewhere. [23,24]

In order to obtain a reliable value of the internal field, one must minimize the contribution of photocarriers to space-charge distribution. To meet this condition, we applied a low intensity narrow laser pulse right after the displacement current. The total charge collected was $\leq 10^{-10}$ C per pulse, and a repetition rate 1 Hz was used to ensure that the diode remained close to its equilibrium state. To perform the null-current method is relatively simple in the case of the Schottky junction because the space-charge-limited current decreases to steady state value. The situation is rather complicated in the case of p-i-n diode, because the recombination current would raise under double injection following the decrease of space-charge-limited current. In order to measure the internal electric field without disturbing by the carrier recombination, one can only

use the time window after the fall of the displacement current and before the rise of the recombination current. The RC constant is < 1 μs and the rise time of the forward-bias recombination current is about 10 μs in this study.

To demonstrate the transient-null-current technique, in Fig. 11 we show the current responses as a function of time from a 0.5 μm a-Si:H p-i-n diode (a) for a 10 μs width positive electrical pulse, V_a, (b) at delay time 1 μs to the electric pulse, the sample is illuminated by a 200 ps width laser pulse, and (c) subtracting (a) from (b) results the net photocurrent response to the laser pulse, j_{pc}. This negative-going photocurrent is due to the photogenerated carriers swept out by the internal electric field. By increasing the voltage of the positive pulse V_a one can null the photocurrent and obtain a certain value of V_a at each wavelength (λ) of the laser pulse. The raw data of V_a vs. λ are related to the internal field profile, $E_i(x)$, in the integral function according to Eq. (7).

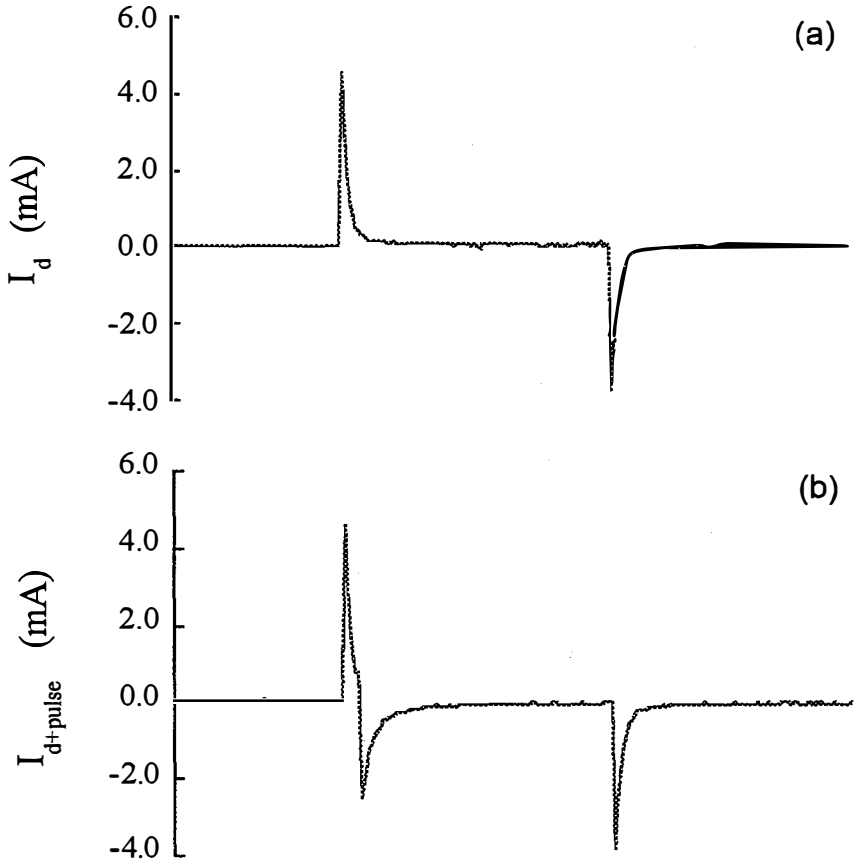

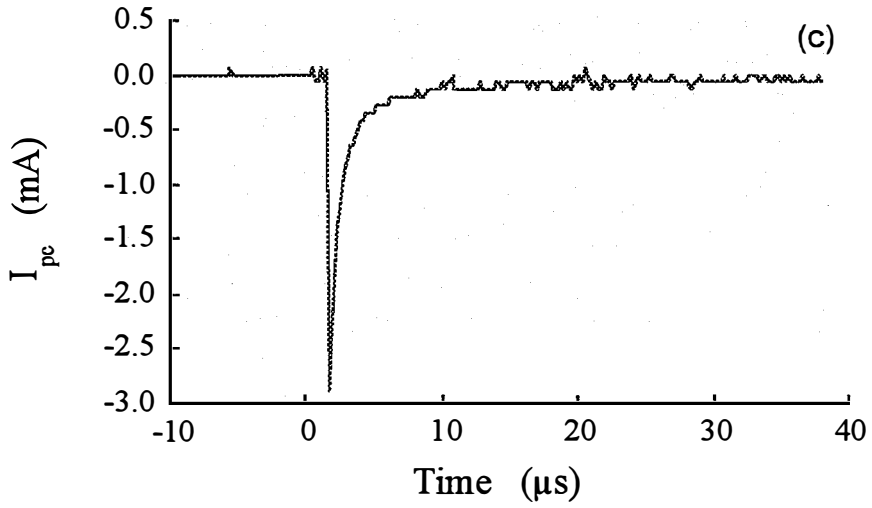

Fig. 11 Current response of a 0.5 μm a-Si:H p-i-n diode for (a) a positive voltage pulse of 0.1 V (b) for both the voltage pulse and laser pulse at l = 630 nm, and (c) the net photocurrent response to the laser pulse, I_{pc} = subtract (a) from (b).

A. The effects of hydrogen dilution on V_{oc} in a-si:h pin solar cells

We studied the effects of H-dilution on V_{oc} in a-Si:H solar cells fabricated by GD CVD.[28] Three types of structures were studied as p-i-n, p-i_H-i-n and p-i_H-n. The J-V characteristics and the internal electric field profile were measured in comparison with the cell performance. We found that H-dilution does stabilize the V_{oc} in both p-i_H-i-n and p-i_H-n structures after 100 hours AM1 light soaking. These two types of H-diluted cells show little changes in current at voltage near V_{oc} before and after light-soaking; while the non H-diluted p-i-n cell does show a noticeable change. A stronger electric field starting from p-i interface is found for both H-diluted cells compared to the non H-diluted p-i-n cell as shown in Fig. 12. Furthermore, there are no measurable changes in the field profile after 100 hour AM1 light-soaking for all three types of cells. All these suggest that an increase of the field strength near p-i interface is crucial for a more stable V_{oc} in H-diluted cells.

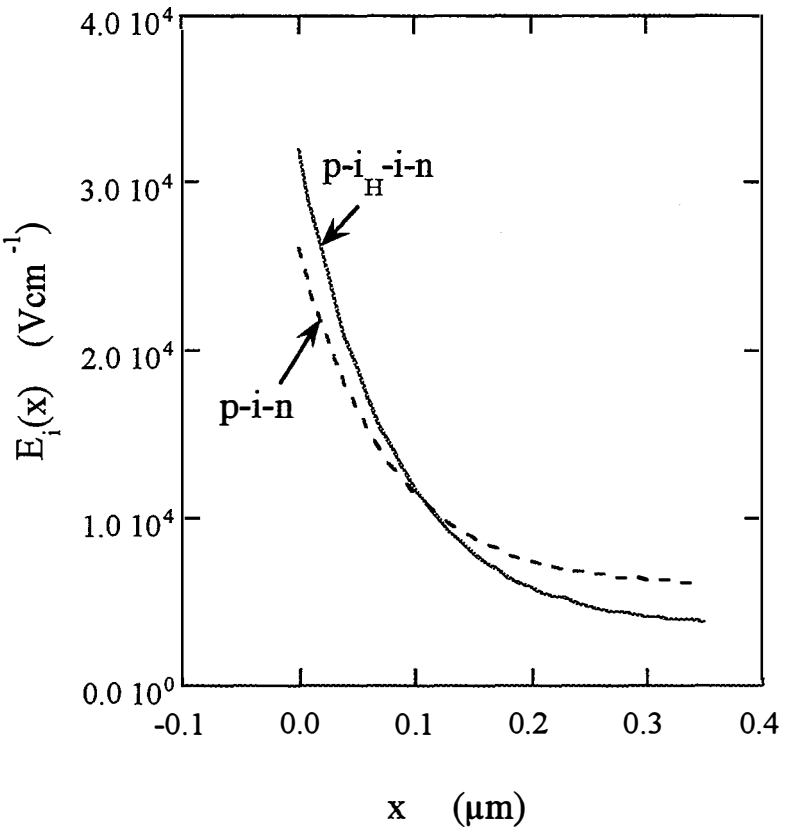

Fig. 12 Internal field profile near p-i interface for p-i-n and p-i_H-i-n structures.

B. Electric field profiles of p-i-n and n-i-p a-Si:H solar cells

It has been found that the cell performance such as the open-circuit voltage, photogain[29,30] et al. depends on the sequence of deposition. We compared the electric field profile of p-i-n and n-i-p structures, and also the light illuminated from the p- or n- side of the same p-i-n cell. In Figs. 13 (a) and 13(b), the V_a vs. λ curves come from glass/TCO/p-i-n/Al and glass/TCO/n-i-p/Al structures made in the same chamber but a different sequence of deposition. The pulse laser light illuminates through the glass side. Interestingly, we obtained the highest V_a in p-i-n but the lowest V_a in n-i-p structure for the shortest wavelength light pulse. The dotted lines in Figs. 13(a) and (b) are the fitting data by using $E_i(x)$ functions that are shown in Figs. 13 (c) and (d) for the F205 p-i-n and F171 n-i-p cells, respectively. It is clear that only the electric field distribution near the p/i interface was obtained for both the p-i-n and the n-i-p cells. Notice, for the n-i-p cell we marked x=0 at the n/i interface.

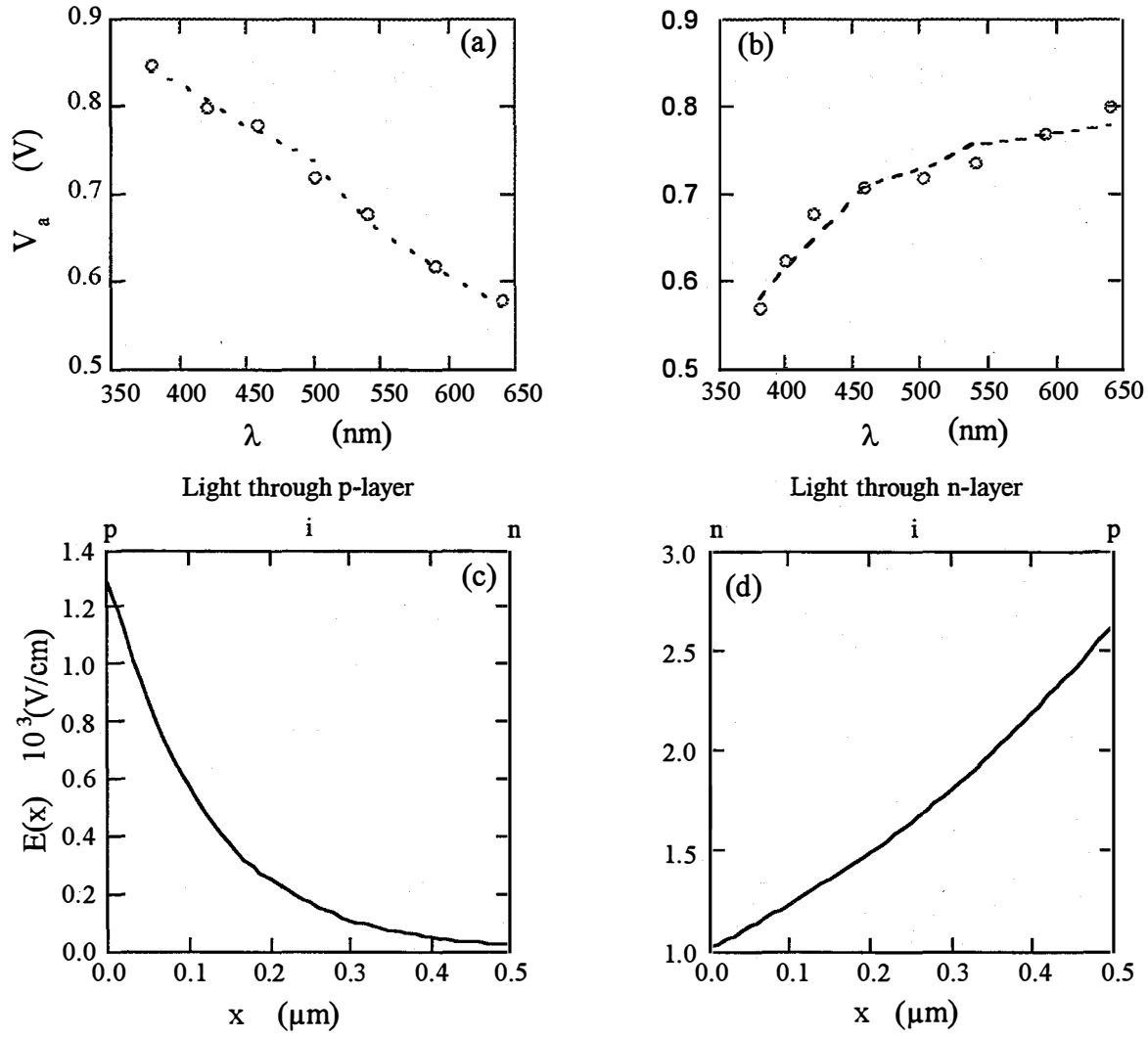

Fig. 13 V_a vs. λ for (a) p-i-n cell F205 light through the p-side, and (b) n-i-p cell F171 light through the n-side. The open circles correspond to the measured V_a and the dotted lines are the best fitting data by using electric field profile $E_i(x)$ in (c) for F205 p-i-n, and (d) for F171 n-i-p cells, respectively.

We further examined the V_a vs. λ by illumination from either the p- or the n- side of the same p-i-n cell with a glass/TCO/p-i-n/TCO structure. The results are plotted in Figs. 14(a), and 14(b). Then the corresponding electric field profiles are given in Figs. 14(c) and 14(d). Notice, we marked x=0 at the n/i interface in Fig. 14(d). Similar to the results from p-i-n and n-i-p cells shown in Figs. 13(c) and 13(d), only the electric field in the vicinity of the p/i interface was deduced by this analysis no matter the light was through p- or n-layer sides for both the p-i-n or n-i-p structures. In fact, as shown in Figs. 14(c) and 14(d), we obtained almost the same electric field profiles near the p/i interface either by illumination through the p- or n-layer of the same cell.

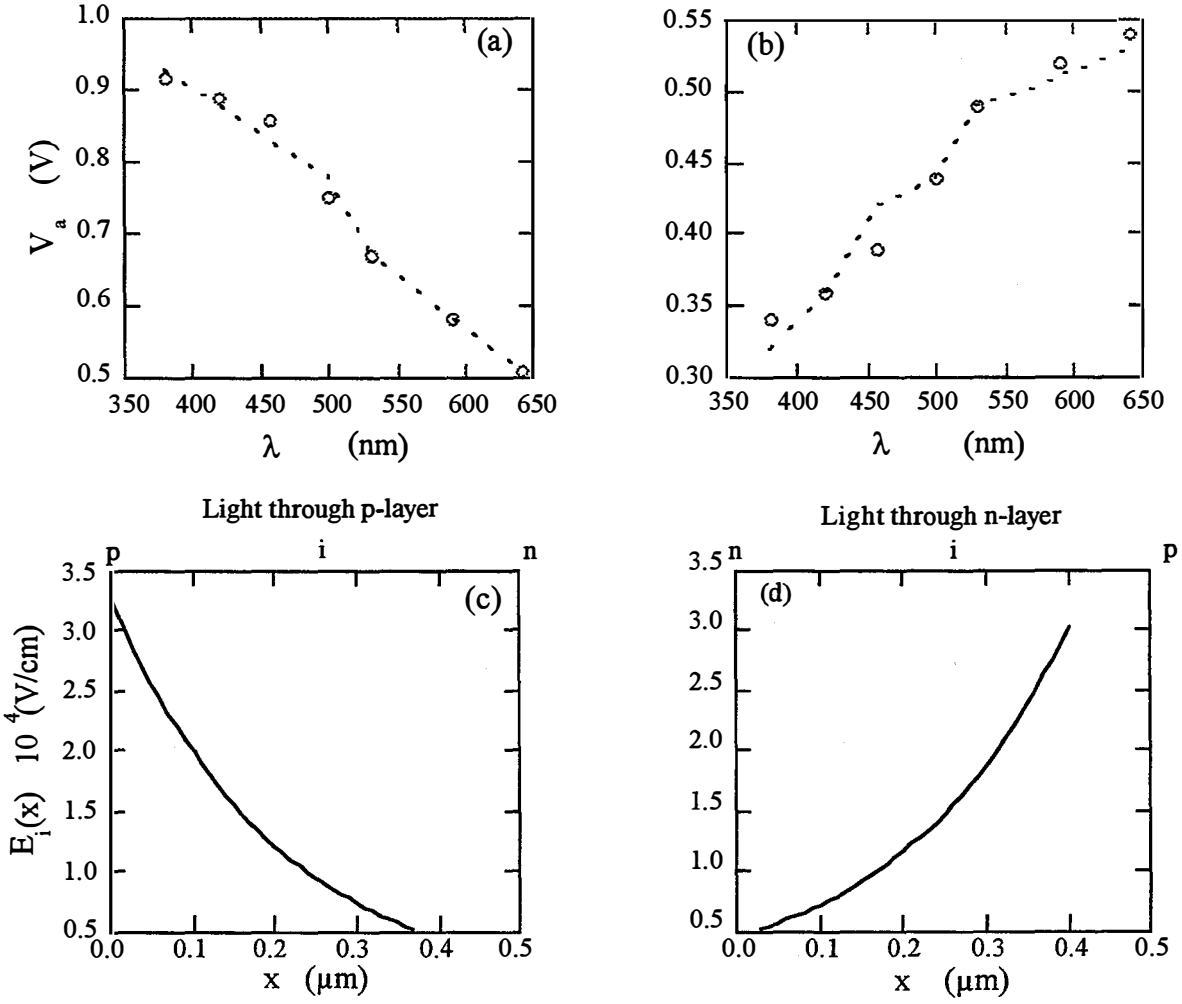

Fig. 14 V_a vs. λ of cell S208 with glass/TCO/p-i-n/TCO structure when light illuminates through (a) the glass side(p-layer), and (b) the top TCO (n-layer). The open circles correspond to the measured V_a and the dotted lines are the fitting data by using electric field profile $E_i(x)$ in (c) and (d), respectively.

We tend to explain the reason why the $E_i(x)$ near p-i junction is reduced by hole limitation as follows. The applied voltage, V_a, is proportional to the peak value of the transient photocurrent j_{pc} which corresponds to the collected photocarrier density per second by the internal field $E_i(x)$. According to the photovoltaic effect, the photogenerated holes will drift towards p-side, and the photo-generated electrons will drift towards n-side in the internal electric field $E_i(x)$. When the short wavelength light illuminates from the p-side, the e-h pairs are generated near the p/i interface due to the shallow absorption depth. The holes will be swiped out through the thin p-layer quickly and the electrons drift oppositely through the i-layer. Since the electron mobility is ten times larger than the hole's, the analysis of Eq. (3) by assuming only electron contribution to the photocurrent is valid. Whereas, as the wavelength increases, the e-h pairs are generated in the bulk of the i-layer and then the hole-limitation effect becomes more and more important, finally becoming dominant. Therefore, the single carrier analysis is no longer valid. Alternatively, when the short wave length light illuminates from the n-layer, the e-h pairs are generated near the n/i

interface. So the holes must travel through the i-layer with a low mobility to be swiped out by the internal field. Thus, the low hole mobility becomes the limitation factor for the photocurrent j_{pc}. In addition, many holes are trapped near the n/i interface and result in a barrier which further depresses the carrier transport. Therefore, one obtains a low j_{pc} as shown in Figs. 13(b) and 14(b). However, as the wavelength increases the hole's travel distance decreases, and then the electron transport becomes more and more important, finally becoming dominant. Therefore, one obtains a larger j_{pc} at a longer wavelength, and the $E_i(x)$ in the vicinity of the p/i interface is obtained.

II.3 Conclusions

In summary, we demonstrated that the experimental knowledge of the internal electric field profile, $E_i(x)$, in thin a-Si:H p-i-n solar cells can be obtained by the transient-null current method, and it can be used to study the effect of a variety of structure designs or processing on the device performance. In order to avoid both space charge contributed by photocarriers and carrier recombination to disturb the internal field, we managed two critical conditions in the measurements: (a) the total charge collected was $\leq 10^{-10}$ C per pulse, and a repetition rate 1 Hz was used to ensure that the diode remained close to its equilibrium state; (b) the width of the laser pulse was 200 ps, and the time window being used was about 1 μs delay following the displacement current to ensure that the transient photocurrent peak was in the time regime of the space-charge-limited-current.

All above results testified that the null-current method is an available technique to measure the internal electric field profile for amorphous silicon p-i-n solar cells. The assumption of electron transport domination is valid in a short wavelength range up to 450 or 500 nm depending on the diffusion length of the minority carrier. Therefore, the present transient null-current technique is available to study the electric profile in the vicinity of the p/i interface for both p-i-n or n-i-p structures. This region indeed is crucial for solar cell performance. The results of the $E_i(x)$ profiles are qualitatively consistent with Hack et al' s computer simulations,[19-21] including the concept of hole-transport limitation. In order to take into account the hole transport limitation in p-i-n structures, more work is needed.

ACKNOWLEDGMENTS

We thank R. Vanderhaghen at Ecole Polytechnique, France for supplying samples. We are grateful for helpful discussions with Steve Hegedus.

III. An NMR investigation of H cluster configurations in a-Si:H

III.1 Introduction

Until very recently, device quality a-Si:H films prepared by conventional glow discharge (GD) technique in different labs exhibited very little difference in structural and physical properties such as the microstructures of hydrogen distribution as detected by nuclear magnetic resonance (NMR). This situation has changed since the demonstration that a-Si:H produced by the hot-wire technique exhibits improved stability; such high quality a-Si:H contains a very low hydrogen content of 2-3 at.% compared to 8-10 at.% in device quality GD a-Si:H. Moreover, there is growing evidence that hot-wire a-Si:H is very different from the GD materials, including the hydrogen microstructures detected by NMR. [31-34] The ^{1}H NMR spectrum of a-Si:H consists of two components, a narrow line with a typical full width at half maximum (FWHM) of a few kHz and a broad line with a typical FWHM of 22 - 35 kHz in GD a-Si:H; this broad line is 50 kHz in hot-wire a-Si:H. Clusters of Si-H have been identified as the origin of the broad component in device quality materials. Previous multiple quantum NMR (MQ NMR) studies suggest that the typical number of hydrogen atoms per cluster is 5 - 7 in device quality GD a-Si:H [31-32] and at least 14 in hot-wire a-Si:H. [33-34] One of the important issues is the nature of these H clusters.

In this work, numerical simulations of free-induction decays (FID) of ^{1}H NMR signals are presented for various H cluster configurations. The observed FID oscillation of the ^{1}H NMR signal in hot-wire a-Si:H is shown to result from a high degree of order in the nearest-neighbor distances between H atoms in the H clusters; such FID oscillation is not visible in GD materials indicating a larger variation in local environment. Numerical simulations of MQ NMR spectra based on several H cluster configurations are also presented. These calculations show that MQ NMR spectra of the relaxed hydrogenated divacancy model fit the observed MQ NMR spectra in device quality GD a-Si:H. These calculations provide restrictions on the possible models of H clusters in a-Si:H. Correlation between the characteristics of these H clusters and the metastability could provide a useful guideline in the search for superior a-Si:H.

III.2 Sample and experimental

Hot-wire a-Si:H samples were made at NREL on Al foil wrapped on a stainless steel substrate at 360 □C. The Al foil was cleaned by first using 2% Micro soap in distilled (DI) water using ultrasound, followed by DI water, acetone, and methanol to rinse, and finally isopropanol vapor cleaning and N_2 gas drying. GD samples were made at Solarex. The a-Si:H films were removed by dilute HCl etching and rinsed by DI water, then vacuum-sealed in 4 mm o.d. ESR quartz tubes.

Two aspects of the H microstructures which were investigated in our experiments are the cluster sizes (i.e., the number of H atoms per cluster), estimated by the multiple-quantum NMR (MQ NMR) technique, and the separation distance of neighboring H atoms, based on intrinsic linewidth measurements and MQ NMR. A home-built, low ^{1}H background NMR probe was used for all NMR measurements. Except for a few spectra taken with a Bruker spectrometer at 4.7 Tesla, all NMR results were obtained using a Chemagnetics spectrometer at 9.4 Tesla. The applied field varied less than 0.05 ppm over the sample volume.

The presented NMR spectra of the hot-wire a-Si:H were taken from a 2 mm thick a-Si:H film deposited on Al foil at a substrate temperature T_s of 360°C. The H content was found to be 2-3

at.% as determined by infrared (IR) spectroscopy and H evolution. The NMR results of the GD a-Si:H were obtained from a sample deposited at $T_s = 250^oC$ on an Al foil by standard d.c. GD decomposition of pure silane; the H content in this sample was 8-10 at.% as determined by IR. For NMR measurements, the Al substrates were removed by HCl etching and the samples were vacuum-sealed in ESR quartz tubings. All experimental results, obtained using a Chemagnetics spectrometer at 9.4 Tesla, were published previously and the pulse sequence used for MQ NMR experiments was discussed previously [33,34]. The pulse width used in the MQ NMR experiments is 1 μs.

III.3 NMR Results of H cluster configurations in a-Si:H

Figure 15 (a) shows the FID's of the hot-wire and the GD samples. Both FID's consist of a rapid intensity decay in the initial 40 μs followed by a slow decay. The initial rapid decay is attributed to Si-H clusters whereas the slow decay is attributed to dispersed Si-H bonds [35,36]. An interesting feature is the oscillatory behavior of the FID signal F(t) near t = 25 μs in the hot-wire sample. Subtracting the component of the slow decay, the intensity of the rapidly decaying component is seen to approach first a minimum (negative or close to zero) near t = 25 μs, recovers slightly after that, and then finally decays to zero at longer t. This behavior is more apparent in the expanded linear plot of FID shown in Fig. 15 (b). Such oscillatory behavior is less obvious in the FID of the GD sample.

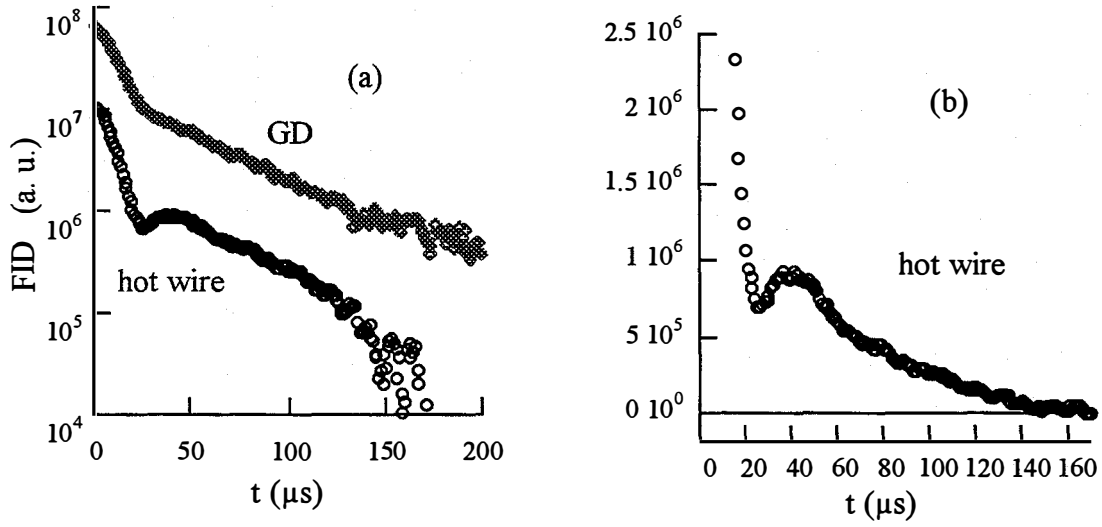

Fig. 15 (a) FID's of ^1H signals in GD and hot-wire a-Si:H films. (b) Expanded linear plot of the FID of the hot-wire sample.

It is now well-established that the internal spin Hamiltonian for ^1H in the H clusters is dominated by the ^1H homonuclear dipolar interaction H_D [31,32]. This interaction governs the evolution of the FID associated with H clusters and is generally a many-body interaction for systems with more than two spins. The evolution of the spin quantum states, which are needed for the calculation of the FID signal, can be calculated numerically for finite spin systems (up to about 10 spins with current computers). It is well known that dipolar interaction leads to oscillatory behavior in the

FID of spins occupying a cubic lattice such as ^{19}F in a CaF_2 crystal [37] It was found semi-empirically that the FID of ^{19}F in a CaF_2 crystal can be described by the function [37],

$$F(t) = \exp(-a^2t^2/2)\frac{\sin(bt)}{bt}, \qquad (8)$$

where the parameters a and b are determined by the second and fourth moment M_2 and M_4, respectively. This oscillatory behavior described by $\sin(bt)$ is not a unique feature of the infinite cubic lattice.

Figure 16 shows the calculated FID's for a cubic and a relaxed hydrogenated divacancy configuration. The cubic configuration is an eight spin system where the spins occupy the 8 corners of a cube. The size of the cube is adjusted so that the calculated full width at half maximum (FWHM) s of the NMR spectrum, given by [38]

$$\sigma(\text{kHz}) = 190\left(\frac{1}{N}\sum_{i,j=1}^{N} 1/r_{ij}^6\right)^{1/2}, \qquad (9)$$

is equal to the FWHM indicated in Fig. 16. These FWHM values are comparable to the experimentally observed widths of ^1H spectra [33,34] In Eq. (9), r_{ij} is the distance between nuclei i and j in unit of Å, and N is the number of interacting spins. Each of the calculated FID in Fig. 16 is an average of calculated FID's over 32 randomly chosen orientations. This is necessary for interpreting data in polycrystalline or amorphous systems. In the calculated FID's for the cubic configuration shown in Fig. 16 (a), oscillations are clearly visible. The first minimum (negative) of F(t) is mainly determined by the interactions among nearest neighbor spins. The pattern of F(t) does not depend on the size of the cube except as a scaling of the time axis proportional to the strength of H_D. Obviously, the timing of the first F(t) minimum depends less sensitively on the strength of H_D than the later oscillations. A small-size change of the cube from 1.915 to 2.156 Å changes the FWHM from 50 to 35 kHz; the corresponding FID's are shown in Fig. 16 (a) as well as the sum of the two FID's. It is interesting to note that the magnitude of the oscillations is reduced significantly through destructive interference. It is worth mentioning that this basic feature of the FID is not a special feature of cubic symmetry; a trigonal configuration would also produce similar features. The cubic configuration captures some of the features of the observed FID in hot-wire a-Si:H shown in Fig. 15. Although this does not identify the nature of the H clusters, it illustrates an important point that a high degree of order is needed to preserve the FID oscillations; large variations of cluster configurations would wipe out the oscillations through destructive interference.

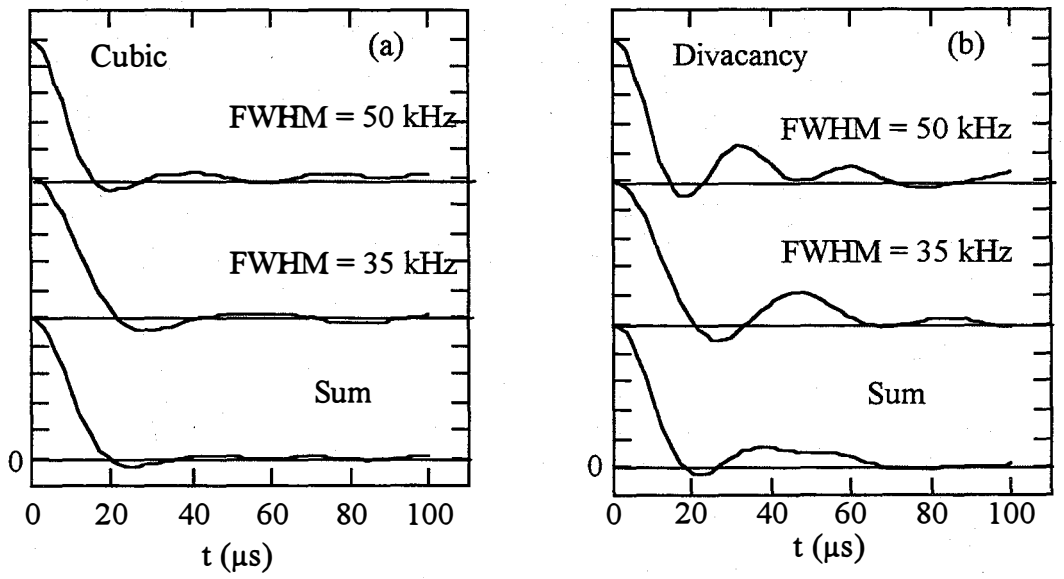

Fig. 16 The calculated FID's for the cubic (a) and the relaxed hydrogenated divacancy (b)configurations. The intensity scale is linear. All FID's are powder averages over 32 random orientations.

Figure 16 (b) shows the FID's of a relaxed hydrogenated divacancy model. A crystalline divacancy is adopted for this model with the six dangling bonds being saturated by H with a Si-H bond length of 1.48 Å. In order to achieve the desired FWHM for simulations, each of the six H atoms was moved from the unrelaxed position along the Si-H bond direction toward the corresponding Si. The displacements are 0.348 and 0.208 Å for s = 35 and 50 kHz, respectively. Figure 16 (b) shows the FID's of this relaxed hydrogenated divacancy model for s = 35 and 50 kHz. Again, the oscillations are present and the sum of these two FID's, also shown in Fig. 16 (b), exhibits the first F(t) minimum determined mainly by the nearest neighbor interactions as well as the rise of intensity above zero. This calculated FID captures the essence of the observed FID in the hot-wire a-Si:H. The calculated FID associated with a relaxed hydrogenated trivacancy model shows similar features as the divacancy model. This is because six out of the eight spins in the trivacancy model have the same nearest neighbor environment as in the divacancy model. Similar FID's are also expected for other hydrogenated multi-vacancies. Hydrogenated vacancy-like defects in an amorphous network could be considerably different from the vacancy models discussed here depending on the randomness and structural relaxation.

Previous MQ NMR results were discussed in terms of an assumed Gaussian distribution of the quantum coherence intensities [31,32]. However, the validity of such a Gaussian distribution function is not guaranteed quantitatively. Moreover, such a description does not give any kinetic information concerning the growth rate of multiple quantum coherence. No specific information was given in terms of the typical distances between H atoms in the H clusters. It is important to realize that the MQ pulse sequence with 8 preparation pulses per cycle works ideally only for systems with dipolar couplings much smaller than $1/t_c$ where t_c is the time duration per cycle (8 pulses) [39]. Realistic experimental conditions such as the finite pulse width (1 μs in the current experiment) does not allow reduction of t_c much less than the employed value (36 μs) in the current experiment. Under the condition that the dipolar couplings are comparable or larger than $1/t_c$, the outcome of the MQ results depends sensitively on the details of experimental conditions

such as the width of the 90° pulses. This is the situation for H clusters in a-Si:H. Reliable predictions can only be made through exact calculations. In the calculations of the MQ spectra presented below, the evolution of the spin system is governed both by the interaction with the rf field and the dipolar interaction when the rf field is on; between the pulses, the evolution of the spin system is governed by the dipolar interaction only. Although the employed MQ pulse sequence is an even order selective sequence for delta 90° pulses, such selectivity breaks down for finite 90° pulses and odd numbered quantum coherence can also appear in the MQ spectra. Each of the calculated MQ spectra shown below is an average of calculated MQ spectra over 32 randomly chosen orientations.

Figure 17 (a) shows the MQ spectra of the GD a-Si:H. The employed cycle time t_c is 36 μs and the pulse width is 1 μs. By increasing the number of times (l_c) the basic 8 pulse preparation cycle is repeated, higher order quantum coherence can be enhanced. The employed l_c values in the experiments are indicated in Fig. 17 ranging from 1 to 16. Figure 17 (b) shows the calculated MQ spectra for a cubic configuration with edge length 2.156 Å to give the FWHM s = 35 kHz. In the calculated spectra, the development of the n = 4 quantum coherence is already apparent in the l_c = 1 case and the n = 6 quantum coherence is clearly visible in the l_c = 2 case. Such rapid development of n = 4 and 6 quantum coherence seems to be slightly faster than in the observed MQ spectra. For l_c = 16, the n = 8 quantum coherence has an intensity comparable to the n = 1 quantum coherence. Using the criteria that odd numbered quantum coherence serves as a measure of noise level in experimental MQ spectra, the maximum number of experimentally observable quantum coherence order should be six for this size cubic configuration after 16 cycles. The cubic configuration reproduces the main features of the observed MQ spectra shown in Fig. 17 (a). Figure 17 (c) shows the calculated MQ spectra for a relaxed hydrogenated divacancy model which gives s = 35 kHz as discussed above. The growth rate for the n = 2, 4, and 6 quantum coherence is very similar to that for the observed MQ spectra shown in Fig. 17 (a). For instance, the n = 4 quantum coherence is barely visible in the calculated and observed MQ spectra with l_c = 1. However, it appears in the calculated and observed MQ spectra with l_c = 2.

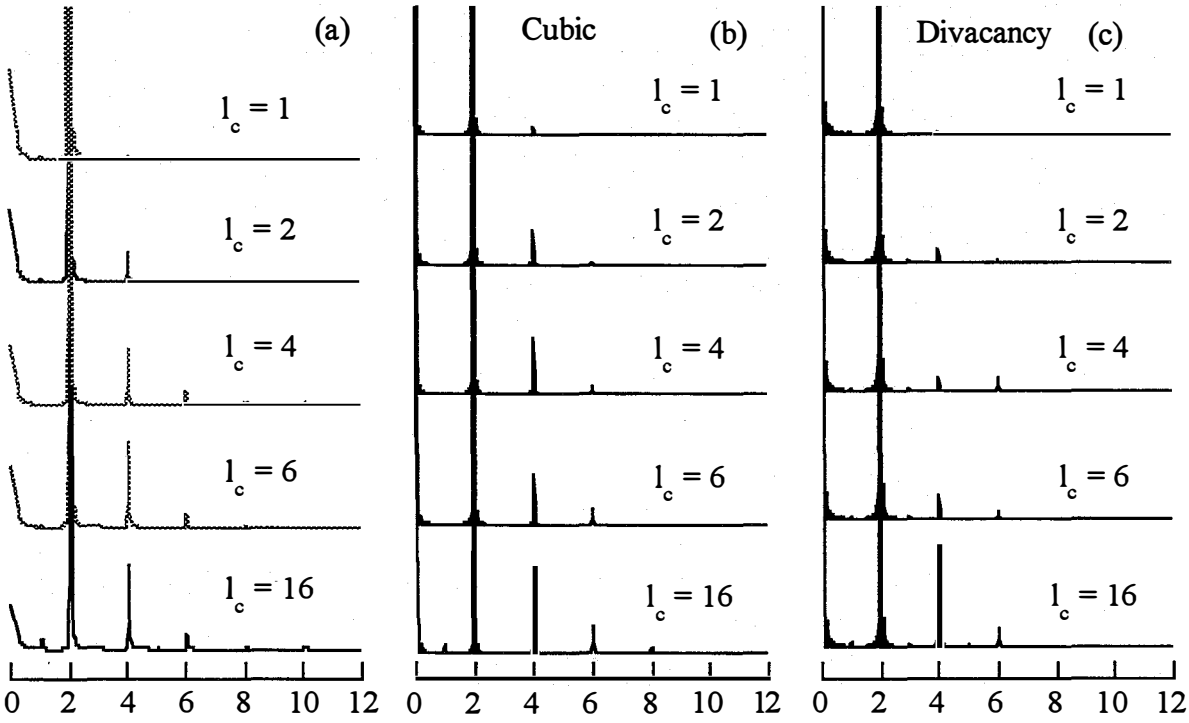

Fig. 17 Observed MQ spectra in GD a-Si:H (a) and calculated MQ spectra based on the cubic (b) and the relaxed hydrogenated divacancy (c) configurations. The horizontal axis labels the order of the MQ coherence and l_c is the number of cycles applied. The preparation time per cycle, t_c, is 36 μs and the 90° pulse width is 1 μs.

The n = 6 quantum coherence emerges above the "noise level" in the calculated and observed MQ spectra with $l_c = 4$. The calculation shows that MQ spectra based on the relaxed hydrogenated divacancy model describe very well the observed MQ spectra in GD a-Si:H. Since other pulse imperfections such as pulse-shape distortions are not incorporated in the calculations, agreement is expected to be less for large l_c values. Since calculations for more than 10 spins are not practical, no attempt was made to explain the MQ spectra of hot-wire a-Si:H which contains larger H clusters [33,34]. A plausible model is the relaxed hydrogenated multivacancies.

In the hydrogenated divacancy model, the six H atoms are separated into two groups, each containing three H atoms. The distance between two H atoms within the group is about 1.989 Å and is about 3.364 Å (or 3.908 Å) between atoms in different groups. To build n = 4 and 6 quantum coherence, coherence between spin states associated with both groups of H atoms are required. The rate of such higher order quantum coherence growth is thus limited by the weak dipolar couplings between the two groups of spins. On the other hand, the strong interaction among spins within each group and the finite width of the 90° pulses hinders the observation of higher order quantum coherence which involve weaker dipolar couplings. Thus, further separation (beyond 4 Å) of these two groups of spins will eliminate the growth of higher order quantum coherence. This is the reason why high-order quantum coherence grows faster in the cubic configuration than in the relaxed hydrogenated divacancy configuration. This shows that a divacancy-like H cluster with separations larger than 4 Å between spins cannot be considered as one cluster in terms of MQ NMR conducted using realistic pulse conditions. The explanation of

the MQ NMR spectra in a-Si:H depends not only on the typical number of H atoms per cluster, but also depends on the internal structure of the clusters.

III. 4 Conclusion

In summary, computer simulations of the observed free-induction decays of the ^{1}H NMR signals indicate that the distribution of the nearest-neighbor distances between H atoms in the H clusters is quite narrow in hot filament assisted CVD a-Si:H whereas the distribution is larger in glow discharge a-Si:H. This is clear evidence of improved structural order in hot filament assisted CVD a-Si:H, which is an important factor leading to more stable materials. Computer simulations of the multiple-quantum NMR spectra indicate that a relaxed hydrogenated divacancy and multi-vacancy models capture the essence of the observed FID in the hot-wire a-Si:H a relaxed hydrogenated divacancy configuration leads to good agreement with experimental observations in device quality GD a-Si:H.

IV Film stress measured by the bending effect

IV.1 Introduction

There are two problems for device applications of a-Si:H: first, the photodegradation of electronic properties, commonly referred to as the Staebler-Wronski effect (SWE)[40]; second, the films have high volume stress, hence the films tend to peel off their substrates.[41-44] It was found that the conventional device-quality intrinsic material (i.e., pure silane plasma-enhanced CVD at ~250 □C, 8-10 at.% hydrogen, ~100% bonded as Si-H) has a high compression value of 10^8-Pa (10^3 atm). This material shows photodegradation, but its stabilized properties are still quite good for large area semiconductor devices. The amount of stress depends upon the deposition conditions and the deposition technique, for instance, electron-beam evaporated film shows 10^8-Pa tensile strength, and it was concluded that there is a linear relationship between the total hydrogen content and the mechanical stress for a-Si films. [45] However, it has been unclear whether there is correlation of stress with the photodegradation or not. Stutzmann [41] studied the correlation between stress-induced substrate (500-μm thickness 7059 glass) curvature and the number of photo-induced silicon dangling bonds (DBs) in a group of a-Si:H films with varied thickness deposited under conventional conditions. He found that (a) the stress was highly non-uniform when the film thickness was greater than 0.5 μm, and (b) the number of metastable defects was proportional to the substrate curvature. Therefore, he suggested that the creation of metastable defects occurs mainly in the strained region of the film near the substrate, and breaking of the strained bonds is the origin of the SWE. But, the creation of metastable defects did not lead to measurable changes of the volume stress in his studies. In disagreement with Stutzmann, Guha et al and Kurtz et al. [42,43] found that (a) the stress was uniform throughout the film up to 4 μm thickness, and (b) there was no measurable relationship between stress and the photo-induced degradation. Harbison et al [44] studied the effect of argon dilution on volume stress in a-Si:H films deposited at 250 □C. They found that (a) an abrupt drop from large compressive to near zero stress occurs where columnar growth morphology appears at 2-3 % diluted silane, and (b) high stress is associated with low growth rate and vice versa. They proposed a model to explain the high compressive stress which involves hydrogen or gaseous impurities during growth. Recently, the hot-wire CVD a-Si:H films [46] have shown significant improvement in stability. It has been found that the H microstructure is different in hot-wire and plasma-CVD a-Si:H films.[34] In the device-quality hot-wire a-Si:H, 2-3 at.% H is needed, compared to 8-10 at.% in plasma-CVD samples. Also 90 % of the hydrogen is located in the clustered regions, compared to about 60- 70 % in the plasma-CVD a-Si:H. Moreover, the hydrogen clusters have a typical size larger than 14 H atoms compared to about 6 in GD a-Si:H samples. The NMR results [34] indicate that the H-microstructure may play an important role in metastability in the device-quality films. On the other hand, no study of mechanical stress in the hot-wire films has done yet. The Gifu group recently has innovated the DC optical-cantilever-bending-detection method similar to the atomic-force microscope for the position detection. It was used to detect the photo-induced change of stress in plasma-CVD a-Si:H.[47] In this work, we study the stress in hot-wire a-Si:H films. This is an important issue in order to understand the mechanism of metastability in a-Si:H materials.

IV..I Sample and experiments

One μm-thick a-Si:H films were deposited on 100 μm-thick 2∞20 mm^2 flat quartz substrates by hot-wire CVD techniques. The substrate temperatures during deposition were 280, 320, 360,

400, and 440 □C, and the hydrogen contents were about 8, 6, 2-3, 1-2, and ≤ 1 at.%, respectively. The film growth rate is 6-8 Å/s. The films were also deposited on 7059 glass and crystalline-silicon substrates for conductivity and IR absorption measurements. The film/thin-quartz system bends due to both the film volume stress during the growth process and the difference in the thermal expansion coefficients of the film and the substrate. Fig. 18 show the bending-beam method for a-Si:H/quartz sample. The sample holder was made from super-invar, which has an extremely small thermal expansion coefficient, and its parallel surfaces were fine-machined to ensure that the sample position would be reproducible. A narrow He-Ne laser beam was used as the probe beam. One piece of the quartz substrate without a-Si:H film was used as the zero-bending reference. The stress then can be measured by the angle θ between reflected beams, which gives the curvature, 1/R. The value of the stress, σ, is given by

$$\sigma = \frac{E_s d_s^2}{6(1-\nu)d_f R} \qquad \text{when } d_f << d_s \text{ and } E_f d_f << E_s d_s, \qquad (10)$$

where E_s is Young's modulus, d_s is the thickness and ν the Poisson's ratio of the substrate, d_f is the thickness of the film. The room temperature values of Young's modulus E_s and Possion's ratio ν for the substrate are 73 MPa and 0.17, respectively. In order to obtain a large signal, the detector was located L2=70 cm away from the sample, which had a free length of L1=1.5 cm. The displacement of the beam deflection spot produced by the curved surface of the sample is of the order of centimeters for an initial stress of 100 - 400 MPa. The detection limitation is 5×10^{-6} rad, which corresponds to a small displacement at the edge of the sample, Δy = 70 Å. This allows us to detect ♠ 0.01 MPa of stress in the a-Si:H films by light-soaking. Light-soaking was carried out *in situ* by a 300 mW/cm^2 tungsten halogen light-source through the quartz side. The light-soaking time was controlled by a mechanical shutter.

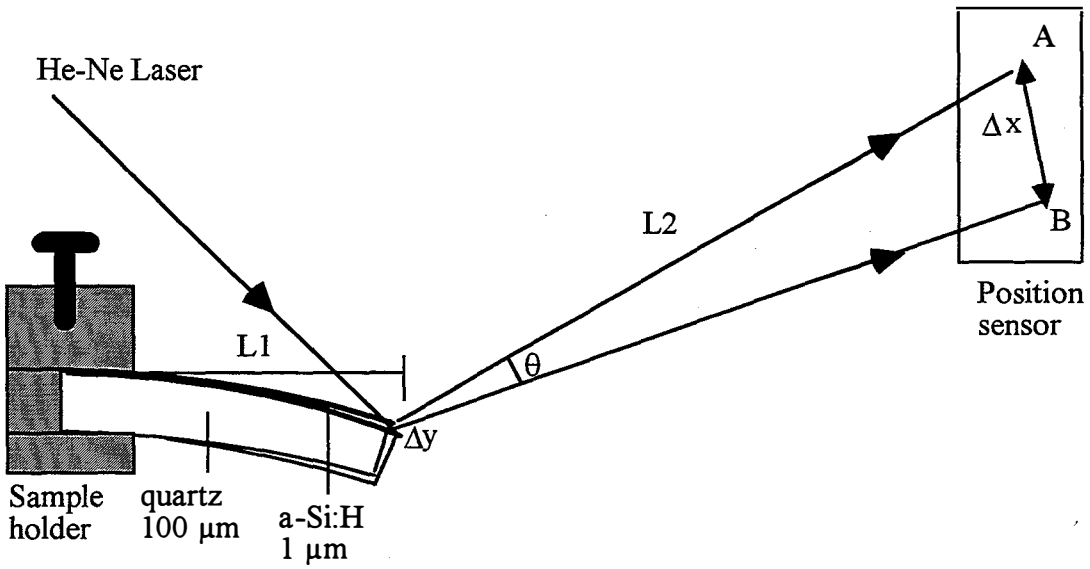

Fig. 18 Schematic diagram of the beam-bending method

VI.3 preliminary results

We show the results of deposition temperature dependence of the film stress in Figs. 19 and 20. The glow-discharge (GD) films were made in Japan at substrate temperature from 100 to 350 □C; the hot-wire (HW) films were made at NREL at 280, 320, 360, 400, and 440 □C. For the GD a-Si:H films, the higher the deposition temperature the higher the compressive stress. Whereas, the stress became tension when the film was annealed at a high temperature of 550 □C, at which the hydrogen effuses out from the film. For the hot-wire films, the deposition temperatures were higher than the GD films. We found that the less hydrogen content the lower the compressive stress in the film as shown in Fig. 20.

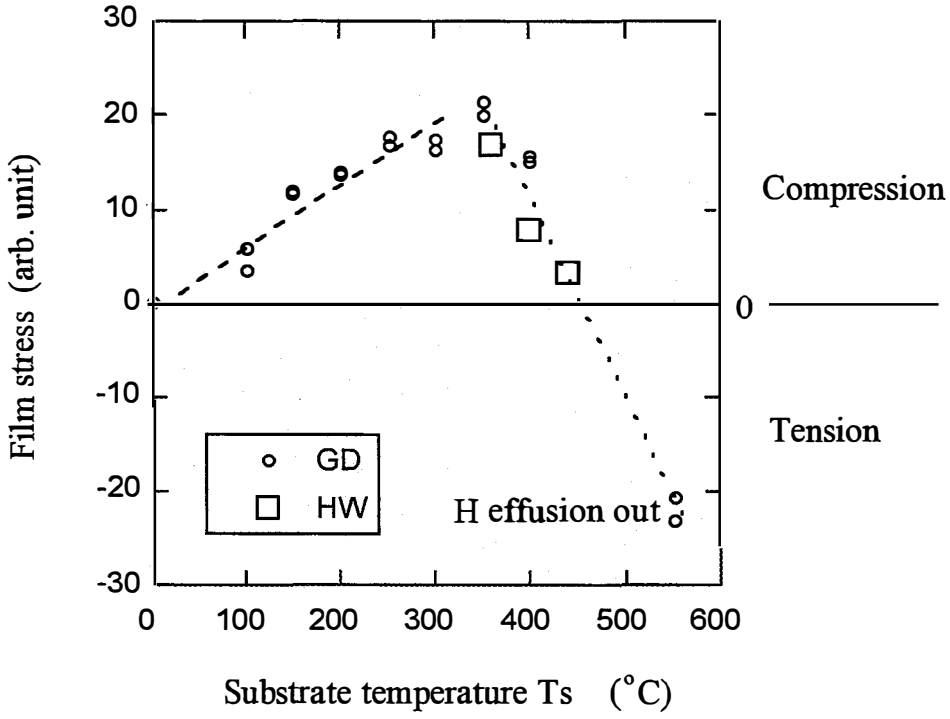

Fig. 19 Deposition temperature dependence of the stress in a-Si:H films measured by the beam-bending method.

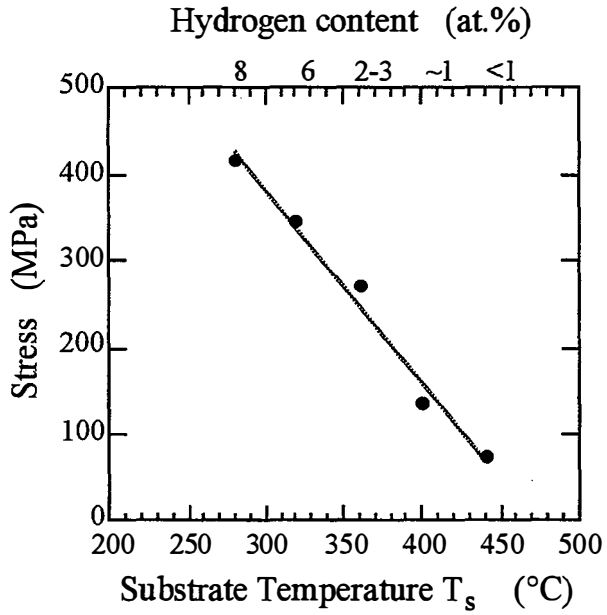

Fig. 20 Deposition temperature dependence of the stress in hot-wire a-Si:H films measured by the beam-bending method.

Acoustic resonance measurements have been made on GD/quartz samples. The resonance frequency increases as the film is light-soaked, which indicates a stiffening of the film according to light-soaking.

Further effort

We have completed the Phase III and the extension period of the research program and met the project goal. This has been accomplished by the EL spectroscopy, the transient-null-current technique, and by NMR and MQ NMR techniques. In addition, we have started the film stress measurements in cooperation with Prof. S. Nitta in Japan. Efforts will be continued to cooperate with team members, especially members from the PV industry to study the factors governing the SWE in a-Si:H solar cells. In the renewed subcontract period, we will pay more attention to the NMR measurements, which give more direct useful information to hydrogen microstructures, and to the internal electric field profile of p-i-n structures.

Publications:

1. Keda Wang, Daxing Han, and M. Silver, "The Power Law Dependence ofEL Intensity on Forward Current in a-Si:H p-i-n Devices", in *Amorphous Silicon Technology*, edited by E. A. Schiff, M.Hack, A. Madan, M. Powell, A. Matsuda, MRS Symp. Proc. **336** 861-866 (1994).
2. Daxing Han and Keda Wang, "A distinct recombination regime in amorphous silicon diodes under double injection", *Appl. Phys. Lett.* **66**, 879-881 (1995).
3. Daxing Han and Keda Wang, "Electroluminescence from hydrogenated amorphous silicon p-i-n diodes" *J. Non-Cryst. Sol.* **190**, 74-84(1995).
4. Regis Vanderhaghen and Daxing Han, "Interface effects on double injection current and photocurrent in a-Si:H n-i-p and p-i-n diodes", *J. Non-Cryst. Sol.***190**, 95-105 (1995).
5. B. Yan, G.J. Adrianenssens, A. Eliat, and D. Han, "Forward current transients in amorphous silicon p-i-n structures", *J. Non-Cryst. Sol.* **190**, 85-94 (1995).
6. Keda Wang and Daxing Han, "Relation of the EL measurements to solar cell parameters", in *Amorphous Silicon Technology*, edited by E.A. Schiff, M. Hack, A. Madam, M. Powell, A. Matsuda, MRS Symp. Proc.**377** (1995) 633.
7. C.N. Yeh, D.X. Han, K.D. Wang and L.E. McNeil, "Carrier recombination in a-Si:H p-i-n devices studied by PL and EL spectroscopies", in *Amorphous Silicon Technology,* edited by E.A. Schiff, M. Hack, A. Madan, M. Powell, A. Matsude, MRS Symp. Proc.**377** (1995) 281.
8. Baojie Yan, Daxing Han, and G.J. Adrianenssens, "Analysis of post-transit photocurrents and electroluminescence spectra from a-Si:H solar cells", J. Appl. Phys. **79** (1996) 3597.
9. Chen-Nan Yeh, Qi Wang, and Daxing Han, "The effect of hydrogen dilution near the p/i interface region on DOS profile in a-Si:H p-i-n solar cells", Amorphous Silicon Technology-1996, edited by M. Hack, E. A. Schiff, M. Powell, A. Matsuda, and A. Madan (MRS Symposium Proc., **420**, 1996), pp. 63-68.
10. J. Todd. Stephen, Daxing Han, Harv Mahan, and Yue Wu, "Hydrogen distribution in high stability a-SI:H prepared by the hot wire technique", ibid, pp.485-490.
11. Daxing Han, Keda Wang, and Liyou Yang, "Recombination and metastability of amorphous silicon solar cells made with and without hydrogen dilution studied by Electroluminescence spectroscopy", J. Appl. Phys. **80** (1996) 2475.
12. Y. Wu, J. Todd. Stephen, Daxing Han, J.M. Rutland, R. A. Crandall, and H. Mahan, "A new hydrogen distribution in a-SI:H: an NMR study", Phys. Rev. Lett., **77** (1996) 2049.
13. Daxing Han, Keda Wang, and Bolko von Roedern, Dispersive-transport-controlled luminescence in hydrogenated amorphous silicon, Phys. Rev. lett., **77**, (1996) 4410.
14. Daxing Han, Keda Wang, Chenan Yeh, Liyou Yang, Xunming Deng, and Bolko Von Roedern, "Luminescence in amorphous silicon p-i-n diodes under doulble injection" Phys. Rev. B **55** 15 619 (1997).
15. The effect of hydrogen dilution on V_{OC} in a-Si:H pin solar cells, Qi Wang, R. S. Crandall, and Daxing Han, Amorphous Silicon Technology-1997, edited by S. Wagner, M. Hack, E. A. Schiff, R. Schropp, and I. Shimizu (MRS Symposium Proc. **467**), pp. 753-758.
16. Internal electric field profile in thin film hydrogenated amorphous silicon diodes studied by the transient-null-current method, Daxing Han, C.N. Yeh, Keda Wang, and Qi Wang, Amorphous Silicon Technology-1997, edited by S. Wagner, M. Hack, E. A. Schiff, R. Schropp, and I. Shimizu (MRS Symposium Proc. **467**), pp. 729-734.
17. An NMR investigation of H cluster configurations in a-Si:H, J.T. Stephen, J. M. Rutland, Daxing Han, and Yue Wu, Amorphous Silicon Technology-1997, edited by S. Wagner, M. Hack, E. A. Schiff, R. Schropp, and I. Shimizu (MRS Symposium Proc. **467**), pp.159-164.

18. Localized states related to oxygen molecules intercalated into C_{70} films, H. Habuchi, D. Han, S. Nitta, T. Itoh, T. Gotoh and S. Nonomura, THE 3rd INTERNATIONAL WORKSHOP IN FULLERENES AND ATOMIC CLUSTERS -- IWFAC '97, June 30 - July 4, 1997, St. Petersburg, Russia.
19. Gas effusion spectra and electric conductivity of O2-intercalated C70 solids, Ryo Yasuda, Daxing Han Takashi Itoh, Shigeru Yoshida, Shoji Nitta, and Shuichi Nonomura, Japanese Symposium on Fullerenes, 1997.7.
20. Daxing Han, Hitoe Habuchi, and Shoji Nitta, Temperature dependence of conductivity and the effect of oxygen intercalation in C_{70} film, Phys. Rev.B **57**, 3773 (1998).
21. Correlation of stress with hydrogen micro-structure in Thin Film Hydrogenated Amorphous Silicon, presented in MRS-97 fall meeting (Dec. 1-5, 1997, Boston), Daxing Han, T. Gotoh, Motoi Nishio, S. Nonomura, S. Nitta, E. Iwaniczko.
22. Tamihiro Gotoh, Shuichi Nonomura, Hideki Watanabe, Shoji Nitta, and Daxing Han, Optical absorption edge temperature dependence of C_{60} films, to be published in Phys. Rev. B.

References

1. D.X. Han, L.E. McNeil, K.D. Wang, C.N. Yeh, Annual Subcontract Report (1 March 94-31 March 95), NREL/TP-411-8116, Aug. 1995.
2. D.X. Han, Annual Subcontract Report (1 April 95-30 June 96), NREL/SR-520-21928, Oct. 1996.
3. M. Silver, D.X. Han, K.D. Wang, M. Kemp, Final Subcontract Report (1 Feb. 91-31 Jan. 94), NREL/TP-451-6491, July 1994.
4. T. S. Nashashibi, I. G. Austin, T. M. Searle, R. A. Gibson, W. E. Spear, and P. G. Le Comber, Philos. Mag. **B45**, 553 (1982).
5. R. Carius, "*Amorphous Silicon Technology,*" edited by E. A. Schiff, M. J. Thompson, A. Madan, K. Tanaka, P. G. LeComber, (MRS Symp. Proc. **297** Pittsburgh, PA, 1990) pp. 101-106.
6. T. M. Searle, M. Hopkinson, W. A. Jackson, A. J. Rhodes, and G. K. Diprose, Phil. Mag. **B63**, 179 (1991).
7. R. A. Street, *Hydrogenated Amorphous Silicon,* (Cambridge University Press, Cambridge, 1991), chapters 4, 6-8.
8. R.W. Collins, M.A. Paesler, and W. Paul, Solid State Commun. **34**, 833, (1980); R. W. Collins and William Paul, Phys. Rev. **B25**, 5257 (1982).
9. W. Fuhs, K. Jahn, in Amorphous Silicon and Related Material edited by H. Fritzsche, World Scientific Publishing, 1988) pp.767-778.
10. B.I. Shklovskii, H. Fritzsche, and S.D. Baranovskii, Phys. Rev. Lett. **62,** 2989 (1989).
11. Daxing Han and Keda Wang, J. Non-Cryst. Solids, **190**, 74 (1995).
12. Daxing Han, Keda Wang, and Bolko von Roedern, Phys. Rev. lett., **77**, (1996) 4410.
13. Daxing Han, Keda Wang, Chenan Yeh, Liyou Yang, Xunming Deng, and Bolko Von Roedern, "Luminescence in amorphous silicon p-i-n diodes under doulble injection," Phys. Rev. B **55** 15 619 (1997).
14. Daxing Han and Keda Wang, and Liyou Yang, J. Appl. Phys., **80**, 2475 (1996).
15. T. Tieje and A. Rose, Solid State Commun. **37**, 49 (1980).
16. J. Orenstein and M. Kastner, Phys. Rev. Lett. **46**, 1421 (1981).
17. Don Monroe, Phys. Rev. Lett. **54**, 146 (1985).
18. J. M. Marshall, R. A. Street and M. J. Thompson, Phil. Mag. **B54**, 51 (1986).
19. M. Hack and M. Shur, J. Appl. Phys.**58**, 997(1985)
20. M. Hack and M. Shur, J. Appl. Phys. **55**, 4413 (1984).
21. M. Hack and M. Shur, J. Appl. Phys. **58**, 1656 (1985).
22. J.K. Arch, F.A. Rubinelli, J.-Y. Hou, and S. J. Fonash, J. Appl. Phys., **69**, 7057 (1991).
23. T. Datta and M. Silver, Appl. Phys. Lett. **38**, 903 (1981).
24. Qi Wang, Keda Wang, C.N. Yeh, and Daxing Han, Amorphous Silicon Technology-1997, edited by M. Hack, E. A. Schiff, R. Schropp, and I. Shimizu (MRS Symp Proc.)
25. R. Konenkamp, S Muramatsu, H. Ioth, S. Matsubara, Appl. Phys. Lett., **57**, 478 (1990).
26. R. A. Street, Phys. Rev B. **27**, 4924 (1983).
27. Sakata.I. and Y.Hayashi, Appl. Phys. Lett. **42**, 279 (1983).
28. Qi Wang, R. S. Crandall, and Daxing Han, Amorphous Silicon Technology-1997, edited by M. Hack, E. A. Schiff, R. Schropp, and I. Shimizu (MRS Symposium Proc.)
29. M.K. Han and W.A. Anderson, Technical Digest of International Electron Device Meeting(Washington), (34)1981
30. Regis Vanderhaghen and Daxing Han, *J. Non-Cryst. Sol.***190**, 95-105 (1995).

31. J. Baum, K. K. Gleason, A. Pines, A. N. Garroway, and J. A. Reimer, Phys. Rev. Lett. **56**, 1377 (1986);
32. K. K. Gleason, M. A. Petrich, and J. A. Reimer, Phys. Rev. B **36**, 3259 (1987).
33. J. Todd Stephen, Daxing Han, Harv Mahan, and Yue Wu, in Amorphous Silicon Technology, edited by M. Hack, E. A. Schiff, M. Powell, A. Matsuda, and A. Madan (Mater. Res. Soc. Proc. **420**, San Francisco, CA, 1996), pp. 485-490.
34. Y. Wu, J. T. Stephen, D. Han, J. M. Rutland, R. A. Crandall, and A. H. Mahan, "New Hydrogen Distribution in a-Si:H: An NMR Study", Phys. Rev. Lett. **77**, 2049 (1996).
35. P.C. Taylor, in Semiconductors and Semimetals, vol. **21C**, edited by J. I. Pankove (Academic Press, Inc. 1984), p. 99.
36. J. A. Reimer and M. A. Petrich, in Amorphous Silicon and Related Materials, edited by H. Fritzsche (World Scientific Co. Singapore, 1989), p. 3.
37. A. Abragam, *Principles of Nuclear Magnetism*, (Clarendon Press, Oxford, 1989), p.120.
38. J. B. Boyce and S. E. Ready, Physica B **170**, 305 (1991).
39. K. K. Gleason, Concepts Magn. Reson. **5**, 199 (1993).
40. D.L. Staebler and C.R.Wronski, Appl. Phys. Lett. **31**, 292 (1977).
41. M. Stutzmann, Appl. Phys. Lett. **47**, 21 (1985).
42. S. Guha, W. den Boer, S.C. Agarwal, and M. Hack, Appl. Phys. Lett. **47**, 947 (1985).
43. S. R. Kurth, Y. S. Tsuo, and R. Tsu, Appl. Phys. Lett. **49**, 951 (1986).
44. J. P. Harbison, A.J. Willams, and D.V. Lang, J. Appl. Phys. **55**, 946 (1984).
45. P. Paduschek, CH. Hopfl, and H. Mitlehner, Thin Solid Films **110**, 291 (1983).
46. A. H. Mahan, J. Carapella, B. P. Nelson, R. S. Crandall, and I. Balberg, J. Appl. Phys. **69**, 6728 (1991).
47. T. Gotoh, S. Nonomura, M. Nishio, N. Masui and S. Nitta, Proc of 17th International Conference on Amorphous and Microcrystalline Silicon, in J. Non-Cryst. Sol (1977).

abstract

This report describes continuing studies on electroluminescence (EL), field profile, and hydrogen microstructure by UNC-CH during the third year and the extension period. Based on systematical studies of the EL, we have developed a complete model to explain the unique features of the EL as dispersive-transport-controlled non-geminate recombination processes. This model can explain the main features of the EL, not only in a-Si:H, but also in other types of trap-rich materials. By employing the forward current and EL temperature dependence studies, information of both the localized tail states and the deep defect states in real solar cell structures were obtained concomitantly, that is crucial for the device performance. We have measured the internal electric field profile in p-i-n and n-i-p cells by a null-current method; we studied the structure of the hydrogen clusters in hot-wire a-Si:H films, both theoretically and experimentally, and show a clear evidence of improved structural order in hot-wire a-Si:H, which is an important factor leading to more stable materials. In order to link the film microstructure to the metastability, we also started the film stress measurements.

REPORT DOCUMENTATION PAGE

Form Approved
OMB NO. 0704-0188

1. AGENCY USE ONLY (Leave blank)	2. REPORT DATE	3. REPORT TYPE AND DATES COVERED
	May 1998	Final Subcontract Report

4. TITLE AND SUBTITLE

Experimental Study of the Factors Governing the Staebler-Wronski Photodegradation Effect in a-Si:H Solar Cells; Final Subcontract Report

5. FUNDING NUMBERS

C: XAN-4-13318-09
TA: PV804401

6. AUTHOR(S)

D. Han

7. PERFORMING ORGANIZATION NAME(S) AND ADDRESS(ES)

University of North Carolina
Department of Physics and Astronomy
Chapel Hill, NC 27599-3255

8. PERFORMING ORGANIZATION REPORT NUMBER

9. SPONSORING/MONITORING AGENCY NAME(S) AND ADDRESS(ES)

National Renewable Energy Laboratory
1617 Cole Blvd.
Golden, CO 80401-3393

10. SPONSORING/MONITORING AGENCY REPORT NUMBER

SR-520-24741

11. SUPPLEMENTARY NOTES

NREL Technical Monitor: B. von Roedern

12a. DISTRIBUTION/AVAILABILITY STATEMENT

12b. DISTRIBUTION CODE

UC-1262

13. ABSTRACT *(Maximum 200 words)*

This report describes continuing studies on electroluminescence (EL), field profile, and hydrogen microstructure by the University of North Carolina, Chapel Hill, during the third year and the extension period. Based on systematic studies of the EL, we developed a complete model to explain the unique features of the EL as dispersive-transport-controlled, nongeminate recombination processes. This model can explain the main features of the EL, not only in hydrogenated amorphous silicon (a-Si:H), but also in other types of trap-rich materials. By employing the forward current and EL temperature-dependence studies, information of both the localized tail states and the deep defect states in real solar-cell structures were obtained concomitantly, which is crucial for the device performance. We measured the internal electric field profile in p-i-n and n-i-p cells by a null-current method; we studied the structure of the hydrogen clusters in hot-wire a-Si:H films, both theoretically and experimentally, and show a clear evidence of improved structural order in hot-wire a-Si:H, which is an important factor leading to more stable materials. To link the film microstructure to the metastability, we also started the film stress measurements.

14. SUBJECT TERMS

photovoltaics ; electroluminescence ; hydrogenated amorphous silicon ; recombination processes ; temperature-dependence studies ; modeling

15. NUMBER OF PAGES

51

16. PRICE CODE

17. SECURITY CLASSIFICATION OF REPORT	18. SECURITY CLASSIFICATION OF THIS PAGE	19. SECURITY CLASSIFICATION OF ABSTRACT	20. LIMITATION OF ABSTRACT
Unclassified	Unclassified	Unclassified	UL